Derivation and solution of effective medium equations for bulk heterojunction organic solar cells

G. RICHARDSON[1], C. P. PLEASE[2] and V. STYLES[3]

[1]*School of Mathematics, University of Southampton, Southampton SO17 1BJ, UK*
email: G.Richardson@soton.ac.uk
[2]*Mathematical Institute, University of Oxford, 24–29 St Giles, Oxford OX1 3LB, UK*
email: Please@maths.ox.ac.uk
[3]*Department of Mathematics, University of Sussex, Brighton BN1 9QH, UK*
email: v.styles@sussex.ac.uk

A drift-diffusion model for charge transport in an organic bulk heterojunction solar cell, formed by conjoined acceptor and donor materials sandwiched between two electrodes, is formulated. The model accounts for (i) bulk photogeneration of excitons, (ii) exciton drift and recombination, (iii) exciton dissociation (into polarons) on the acceptor–donor interface, (iv) polaron recombination, (v) polaron dissociation into a free electron (in the acceptor) and a hole (in the donor), (vi) electron/hole transport and (vii) electron–hole recombination on the acceptor–donor interface. A finite element method is employed to solve the model in a cell with a highly convoluted acceptor/donor interface. The solutions show that, with physically realistic parameters, and in the power generating regime, the solution varies little on the scale of the micro-structure. This motivates us to homogenise over the micro-structure; a process that yields a far simpler one-dimensional *effective medium* model on the cell scale. The comparison between the solution of the full model and the effective medium (homogenised) model is very favourable for applied voltages less than the built-in voltage (the power generating regime) but breaks down as the applied voltages increases above it. Furthermore, it is noted that the homogenisation technique provides a systematic way to relate effective medium modelling of bulk heterojunctions [19, 25, 36, 37, 42, 59] to a more fundamental approach that explicitly models the full micro-structure [8, 38, 39, 58] and that it allows the parameters in the effective medium model to be derived in terms of the geometry of the micro-structure. Finally, the effective medium model is used to investigate the effects of modifying the micro-structure geometry, of a device with an interdigitated acceptor/donor interface, on its current–voltage curve.

Key words: Shockley model, drift diffusion, asymptotic analysis, photovoltaic, homogenisation.

1 Introduction

Organic photovoltaics (OPVs) are a relatively new technology [24] that offers the prospect of cheap mass produced solar cells manufactured by printing techniques such as roll to

roll processing [28]. The energy efficiency of these devices has increased rapidly within the past 10 years [13] and they are rapidly approaching the point at which they will be able to compete in the commercial market with standard inorganic devices; currently they have maximum power conversion efficiencies in excess of 13% [13].

Photovoltaics are typically formed from two (or possibly more) semiconducting materials with different electrical properties that give the device the characteristics of a diode. Thus, positive charge carriers (holes) move readily across the device in one direction, but not in the other, while negative charge carriers (free electrons) move easily in the opposite direction, but not in the same direction as the holes. The device functions by absorbing light to create charge pairs (in the form of free electrons and holes) which then separate because the two types of charge carrier move preferentially in different directions. This gives rise to a flux of positive charges onto one electrode and of negative charges onto the other electrode that may be used to drive a current around a circuit.

Here, we outline the important physical processes involved in the operation of OPVs (noting that a detailed review of the physics of can be found in [12, 20]). Charge pair generation typically occurs in a three step process. First, a photon (with an appropriate energy) is absorbed within one of semiconductors to create a tightly bound excited charge complex (exciton). This migrates within the material, by a diffusive process, and may either recombine losing its energy to the device (releasing it as heat or light) or reach the interface between the two semiconductors. If it reaches this interface, it forms a geminate pair that, because of the differences in ionisation potential and electron affinity between the two materials, is much less tightly bound than the exciton and so can separate into a free electron in the acceptor and a free hole in the donor. However, geminate pair recombination is thought to be a significant loss mechanism in organic devices [16, 26]. Once the charges have been separated they can either recombine on the interface (non-geminate pair recombination) or migrate to the contacts where their charge can be harvested to give useful electrical energy. Notably, non-geminate recombination is fairly insignificant at short-circuit ($V = 0$, $J = J_{sc}$) but becomes much more significant towards open circuit ($V = V_{oc}$, $J = 0$) [16] in the regime that a solar cell typically operates.

A significant problem that arises in the design of organic devices is that the diffusion lengthscale of an exciton (i.e., the typical distance an exciton diffuses before it recombines and loses its energy) is much shorter, at around 10 nm [24], than the thickness of semiconductor required to absorb a significant fraction of the incident light, which is about 200 nm [24]. Consequently bilayer devices (see Figure 1(a)), formed from planar slabs of acceptor and donor materials separated by a planar interface, are always very inefficient [47] because if they are thick enough to absorb most of the incident light energy a large majority of the excitons created will be too far from the interface to stand much chance of diffusing to the interface before they recombine. Conversely, a device that is sufficiently thin to allow most of the captured excitons to diffuse to its interface is only capable of absorbing a small fraction of the incident light.

In order to circumvent this difficulty it is customary to make OPVs in the form of *bulk heterojunctions* (see Figure 1(b) and (c)). These devices are sufficiently thick to absorb most of the incident sunlight (>200 nm) but which possesses a highly convoluted acceptor/donor interface with the property that most regions of the device are within an exciton diffusion length of the interface (∼10 nm). Such convoluted interface geometries
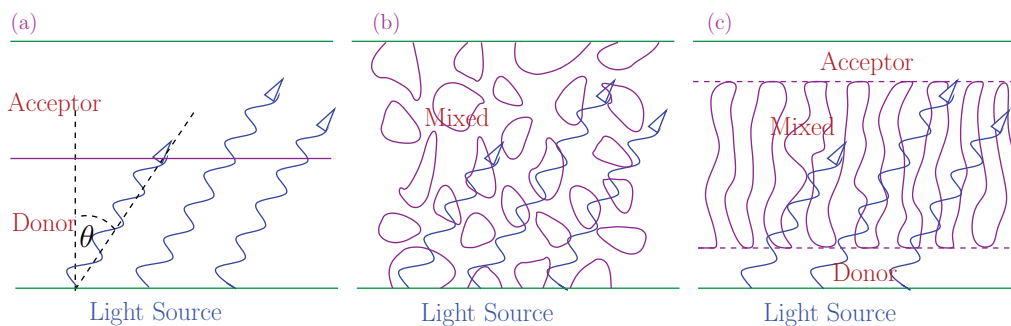
FIGURE 1. Schematic cross-sections of (a) a bilayer device, (b) a bulk heterojunction manufactured by spin-coating, and (c) a bulk heterojunction manufactured by controlled vapour-deposition.

ensure that most of the excitons generated reach the interface and separate into electron hole pairs rather than recombining. Three-dimensional images of bulk heterojunctions, based on scanning electron microscopy and simulations of the annealing process used to form the devices, are shown in [46]. Bulk heterojunctions can either be grown, for example, by spin-coating and phase separation of the acceptor and donor in a drying solution (with subsequent annealing to control domain size) [41] or by controlled organic vapour phase deposition [60]. The former process leads to a uniform mixed thin film in which acceptor and donor regions are intermingled (see Figure 1(b)), whereas the latter can be used to produce a graded thin film in which a mixed layer separates donor and acceptor layers (see Figure 1(c)). A notable advantage of manufacturing a device with capping layers of pure donor and pure acceptor (as illustrated in Figure 1(c)) is that these can block the transport of holes to the upper (electron extracting) electrode and conduction electrons to the lower (hole extracting) electrode. Without capping layers the direction of charge transport in the heterojunction is typically controlled by using electrodes with different work functions [24].

Many theoretical studies of such bulk heterojunction devices have applied drift-diffusion charge transport models to realistic device geometries focussing on the role of the convoluted interface morphology in determining the electrical behaviour and efficiency of the device [8, 35, 38, 39, 58]. Other studies have used effective medium type models in order to obtain a picture of the average electrical behaviour of solar cell on the device lengthscale ($\sim$200 nm) while smearing out the effects of the convoluted interface ($\sim$10 nm) [19, 25, 36, 37, 42, 59]. From a numerical viewpoint it is far easier to solve the one-dimensional partial differential equations (PDEs) that result from pursuing the effective medium approach than the two- or three-dimensional, highly heterogeneous, PDE model that is a consequence of pursuing the more fundamental approach adopted in [8, 35, 38, 39, 58]. Indeed, Kodali *et al.* [35] note that solving over a bulk heterojunction geometry with physically realistic parameters requires the use of an extremely fine grid and parallelised computational methods. However, the effective medium approaches employed in [19, 25, 36, 37, 42, 59] are *ad-hoc* and so unable to relate the coefficients in their equations to the geometry of the micro-structure, or systematically account for the capping layers of

unadulterated donor (or acceptor) material (seen for example in the devices manufactured by [46, 60]).

It remains an open question when, and whether, an effective medium approach is capable of genuinely approximating the full description of the device applied on a real morphology. It is the aim of this work to address this question. We start with a drift diffusion model that was formulated in [21, 49], to describe a bilayer organic solar cell, and validated against real data.[1] We apply this model to a convoluted two-dimensional device geometry and solve it numerically. We then compare the numerical solutions, for the two-dimensional device geometry, to the results of a one-dimensional effective medium model that is systematically derived from the full model by use of homogenisation techniques. The results show that in the power generating regime (the regime of interest) the effective Debye length of the material is large compared to the fine scale morphological structure of the device, and there exists a good agreement between the solution to the full model and the effective medium model. However in sufficiently strong forward bias, the applied voltage exceeds the built-in voltage and there is a build-up in electron and hole density because the electrons are driven away from the acceptor contact and the holes move away from the donor contact. This increase in electron and hole density causes a corresponding decrease in the effective Debye length until eventually it is reduced to the scale of the fine structure and the effective medium approach breaks down. In this limit, we suggest an alternative approach to approximating the full model. We finish by using the effective medium model that we have derived to calculate the profiles of charge carrier densities and the electric potential across the device and to calculate typical current–voltage curves.

Before proceeding with the formulation of drift-diffusion model, we note that there is also a considerable body of literature that investigates charge transport (and generation) in OPVs with Monte-Carlo simulations (see, for example, [26,27,32,44,45]). These simulations are particularly useful for examining the details of phenomena occurring on the molecular scale, such as carrier trapping by heterogeneities in the HOMO[2] and LUMO[3] levels and geminate pair recombination.

2 Model formulation

2.1 Governing equations

We begin by writing down the dimensional equations that model charge transport within the cell and denote all dimensional variables by a $*$ superscript.

2.1.1 *Electron and hole transport in the semiconductors*

Consider a simple drift-diffusion model for the motion of holes and electrons in an organic semiconducting device. This takes the usual form for such devices (see, for

---

[1] This model is similar to the previous drift diffusion models for organic diode [17,18].

[2] Highest occupied molecular orbital: the analogue of the valence band edge in an inorganic semiconductor.

[3] Lowest unoccupied molecular orbital: the analogue of the conduction band edge in an inorganic semiconductor.

example, [8, 17, 18]) with the notable simplifications that there is no doping and that hole density in the acceptor and electron density in the donor are negligible, a result of the large differences in electron affinity and ionisation potential between the acceptor and donor materials. More details are provided in [21, 49]. The model consists of conservation equations for the free electron number density n^* and the hole number density p^*

$$n^* = 0 \quad \text{and} \quad q\frac{\partial p^*}{\partial t^*} + \nabla^* \cdot \boldsymbol{j}_p^* = 0 \quad \text{for} \quad (x^*, y^*) \in \Omega_d, \tag{2.1}$$

$$p^* = 0 \quad \text{and} \quad q\frac{\partial n^*}{\partial t^*} - \nabla^* \cdot \boldsymbol{j}_n^* = 0 \quad \text{for} \quad (x^*, y^*) \in \Omega_a, \tag{2.2}$$

in which $\boldsymbol{j}_p^*$ is the hole current density, $\boldsymbol{j}_n^*$ is the electron current density, and the domains Ω_d and Ω_a are those occupied by the donor and acceptor materials, respectively, as illustrated, for example, in Figure 3.

The motion of both the holes and electrons is assumed to be governed by the standard drift-diffusion model so that the electron and hole current densities are given by

$$\boldsymbol{j}_p^* = -qD_p \left(\nabla^* p^* + \frac{q}{kT} p^* \nabla^* \phi^* \right), \tag{2.3}$$

$$\boldsymbol{j}_n^* = qD_n \left(\nabla^* n^* - \frac{q}{kT} n^* \nabla^* \phi^* \right). \tag{2.4}$$

Here, ϕ^* is the electric potential, k is Boltzmann's constant, T is absolute temperature, and D_p and D_n are the hole and electron diffusion coefficients, respectively.

The electric potential ϕ^* is governed by Poisson's equation, which, on allowing for the difference in permittivity between the two materials, gives

$$\nabla^* \cdot \left(\epsilon_d \nabla^* \phi^* \right) = -qp^* \quad \text{for} \quad (x^*, y^*) \in \Omega_d, \tag{2.5}$$

$$\nabla^* \cdot \left(\epsilon_a \nabla^* \phi^* \right) = qn^* \quad \text{for} \quad (x^*, y^*) \in \Omega_a, \tag{2.6}$$

where ϵ_d and ϵ_a are the permittivities of the donor and acceptor, respectively.

2.1.2 Boundary conditions at the contacts

There are two cases to be considered. In the first of these (illustrated in Figure 1(c)) blocking layers stop contact between the acceptor and the lower (hole extracting) electrodes and between the donor and the upper (electron extracting) electrodes; appropriate Ohmic boundary conditions therefore consist of imposing the electric potential ϕ^* and electron concentration n^* on the upper electrode $(y^* = L)$, whilst imposing ϕ^* and the hole concentration p^* on the lower electrode $(y^* = -L)$ such that

$$\phi^*|_{y^*=-L} = \frac{V - V_{bi}}{2}, \qquad \phi^*|_{y^*=L} = -\frac{V - V_{bi}}{2}, \tag{2.7}$$

$$p^*|_{y^*=-L} = p_-, \qquad n^*|_{y^*=L} = n_+. \tag{2.8}$$

Here, V_{bi} is the built-in voltage across the device at equilibrium, arising from the difference in the Fermi levels of the two semiconductors (in isolation), while V is the applied voltage

across the device, and p_- and n_+ are known constants that depend upon the properties of the contacts, see (2.20) and the discussion preceding it, for further details. In scenarios in which the acceptor contacts the hole extracting lower electrode and the donor contacts the electron extracting upper electrode (as illustrated in Figure 1(b)), the Ohmic boundary conditions on the carrier concentrations (2.7) are replaced by

$$p^*|_{\{y^*=-L\}\cap\Omega_d} = p_-, n^*|_{\{y^*=-L\}\cap\Omega_a} = n_-, p^*|_{\{y^*=L\}\cap\Omega_d} = p_+, n^*|_{\{y^*=L\}\cap\Omega_a} = n_+. \quad (2.9)$$

It will be shown that (2.9) does not provide a particularly good description of the behaviour of devices with the structure shown in Figure 1(b) and corrections to these conditions will be considered in Section 6.

2.1.3 *Exciton generation and recombination in the semiconducting materials*

Excitons are generated on absorption of photons in both donor and acceptor materials, although the rate of photon absorption (and thus also exciton generation) is typically considerably larger in the polymeric donor material than in the acceptor,[4] see, for example, [36, 53]. Thus, if $\mathcal{A}_a$ and $\mathcal{A}_d$ are the fraction of photons absorbed in the acceptor and donor per unit depth of material, and Q^* is the photon flux, then the rate of exciton generation per unit volume is $\mathcal{A}_a Q^*$ in the acceptor and $\mathcal{A}_d Q^*$ in the donor. In order to calculate the photon flux as a function of position across the cell, we average the rate of absorption across the cell from the acceptor and donor. Assuming that these have volume fractions (as a function of depth y^*) of $F(y^*)$ and $1 - F(y^*)$ and that the angle of the incident radiation to the cell surface normal is θ (depicted in Figure 1(a)), the rate of photon absorption per unit width of the cell is $(\mathcal{A}_a F(y^*) + \mathcal{A}_d(1 - F(y^*)))/\cos\theta$. Furthermore, if the incident radiation intensity is Q_0, then the photon flux striking the surface of cell $y = -L$ is $Q_0 \cos\theta$. It follows that Q^* satisfies the following initial value problem in y^*:

$$\frac{\partial Q^*}{\partial y^*} = -\frac{(\mathcal{A}_a F(y^*) + \mathcal{A}_d(1 - F(y^*)))}{\cos\theta} Q^*, \qquad Q^*|_{y^*=-L} = Q_0^* \cos\theta. \quad (2.10)$$

We note that a more comprehensive treatment of light absorption and exciton generation would also account for frequency dependent variations in the absorption spectrum.

Excitons are mobile and diffuse in the device until they either recombine (losing their energy as they do so) or meet the acceptor/donor interface on which they are absorbed and separated into a coulombically bound charge pair on either side of the interface (a geminate pair). Assuming recombination rates of α_a and α_d, in the acceptor and donor regions, respectively, and using similar notation for the exciton diffusion coefficients $\mathcal{D}_a$ and $\mathcal{D}_d$, leads to conservation laws for the exciton number densities c_a^* and c_d^* in the

---

[4] These are frequently formed from a C_{60} compound.

acceptor and donor regions, respectively,

$$\frac{\partial c_a^*}{\partial t^*} = \mathcal{D}_a \nabla^{*2} c_a^* + \frac{\mathcal{A}_a}{\cos\theta} Q^*(y^*) - \alpha_a c_a^* \qquad \text{in} \quad \Omega_a, \tag{2.11}$$

$$\frac{\partial c_d^*}{\partial t^*} = \mathcal{D}_d \nabla^{*2} c_d^* + \frac{\mathcal{A}_d}{\cos\theta} Q^*(y^*) - \alpha_d c_d^* \qquad \text{in} \quad \Omega_d. \tag{2.12}$$

Furthermore, we assume that there is no flux of excitons from the contacts, so that

$$\left.\frac{\partial c_d^*}{\partial y^*}\right|_{y^*=-L} = 0 \qquad \text{and} \qquad \left.\frac{\partial c_a^*}{\partial y^*}\right|_{y^*=L} = 0, \tag{2.13}$$

and that any exciton that reaches the acceptor/donor interface $\partial\Omega_i$ is immediately absorbed (forming a electrostatically bound geminate charge pair) so that

$$c_a^*|_{\partial\Omega_i} = 0, \qquad c_d^*|_{\partial\Omega_i} = 0. \tag{2.14}$$

Here, we denote the sections of the boundaries to Ω_a and Ω_d that are common to both (i.e., the acceptor/donor interface) by $\partial\Omega_i$.

One of the keys to understanding the efficiency of the device is the fate of the geminate charge pairs. These may either recombine (geminate recombination), resulting in the loss of their energy, or separate into a free electron in the acceptor and a free hole in the donor which can be subsequently harvested at the contacts. The theoretical treatment of this process is beyond the scope of this work but we note that there have been a number of works that simulate it via Monte-Carlo methods, see, for example, [26, 27, 44, 57]. The results of these treatments can be summarised by a single parameter γ_{eff}, which gives the fraction of excitons absorbed onto the interface that eventually dissociate into a free electron (in the acceptor) and hole (in the donor). The fate of the remaining fraction $1 - \gamma_{eff}$ is geminate recombination on the boundary. Furthermore, the simulations conducted by Offermans et al. [44] suggest that γ_{eff} is field dependent (larger in reverse bias than forward bias) but that at room temperature this is not a large effect.

2.1.4 *Jump conditions on the donor/acceptor interface $\partial\Omega_i$*

There is assumed to be no significant surface charge on the interface $\partial\Omega$, implying continuity of both electric potential and the normal component of the electric displacement on $\partial\Omega_i$,

$$[\phi^*]_{\partial\Omega_i} = 0, \qquad \left[\epsilon\mathbf{N}\cdot\nabla^*\phi^*\right]_{\partial\Omega_i} = 0. \tag{2.15}$$

Here, $\mathbf{N}$ is the unit normal to the interface (pointing from the donor into the acceptor).

Charge conservation at the interface implies continuity of current across $\partial\Omega_i$, that is,

$$\mathbf{j}_n^* \cdot \mathbf{N}|_{\partial\Omega_i} = \mathbf{j}_p^* \cdot \mathbf{N}|_{\partial\Omega_i}. \tag{2.16}$$

In addition, we need to account for interfacial conservation of electrons and holes. These are created in pairs by the dissociation of excitons (resulting in equal fluxes j_{phot}^*/q of

electrons into the acceptor and holes into the donor) and destroyed (in pairs) by non-geminate recombination (resulting in equal fluxes $R^*(n^*, p^*)$ of electrons onto the interface from the acceptor and holes onto the interface from the donor). These arguments lead to the interfacial conservation laws:

$$\boldsymbol{j}_n^* \cdot \boldsymbol{N}|_{\partial\Omega_i} = \boldsymbol{j}_p^* \cdot \boldsymbol{N}|_{\partial\Omega_i} = qR\left(n^*|_{\partial\Omega_i}, p^*|_{\partial\Omega_i}\right) - j_{phot}^*. \tag{2.17}$$

As noted above generation at the interface occurs as a result of incident excitons forming interfacially bound geminate pairs of which only a fraction γ_{eff} dissociate into an electron a hole, with the remaining fraction $1 - \gamma_{eff}$ undergoing geminate recombination (and losing their energy to heat or light). On accounting for the fluxes of excitons onto the interface, the generated flux j_{phot}^*/q of electrons and holes away from the interface is given by

$$j_{phot}^* = q\gamma_{eff}\left(\mathcal{D}_a\frac{\partial c_a^*}{\partial N^*}\bigg|_{\partial\Omega_i} - \mathcal{D}_d\frac{\partial c_d^*}{\partial N^*}\bigg|_{\partial\Omega_i}\right). \tag{2.18}$$

Here, we consider only a constant rates of geminate recombination but this could easily be modified to cover field dependent rates of dissociation (as described in [5]) by making γ_{eff} a function of the electric field on the boundary.

2.1.5 *The (non-geminate) recombination rate and its relation to thermodynamically consistent Ohmic boundary conditions*

We now examine the model and ensure that the parameters are consistent with the idea that when the device is in equilibrium, detailed balance reinforces no current flow. Typically, recombination rates are modelled by an algebraic expression that depends on local electron and hole concentrations (such as the Shockley Read Hall rate, see, e.g., [42]) that accounts for flow of charge carriers into intermediate trapped states. Here, we write the interfacial recombination in the generic form

$$R\left(n^*|_{\partial\Omega_i}, p^*|_{\partial\Omega_i}\right) = \left(n^*|_{\partial\Omega_i}\, p^*|_{\partial\Omega_i} - N_i^2\right)\Theta\left(n^*|_{\partial\Omega_i}, p^*|_{\partial\Omega_i}\right), \tag{2.19}$$

noting that, at thermal equilibrium, the term $(n^*|_{\partial\Omega_i}\, p^*|_{\partial\Omega_i} - N_i^2)$ ensures a balance between thermal generation and recombination of the form $n^*|_{\partial\Omega_i}\, p^*|_{\partial\Omega_i} = N_i^2$. It is modulated by the function $\Theta(n^*|_{\partial\Omega_i}, p^*|_{\partial\Omega_i})$, which accounts for the particular mechanisms involved in recombination [33]. In all the simulations we present, we consider a Langevin recombination along $\partial\Omega_i$ (as is standard in the literature, e.g., [8, 36]) of the form $R\left(n^*|_{\partial\Omega_i}, p^*|_{\partial\Omega_i}\right) = n^*|_{\partial\Omega_i}\, p^*|_{\partial\Omega_i}\Theta\left(n^*|_{\partial\Omega_i}, p^*|_{\partial\Omega_i}\right)$ in which we neglect the thermal generation term N_i^2 because it is, in physically realistic regimes, vanishingly small.

In order for the device to have an equilibrium that satisfies detailed balance, there must be a solution $(n_{eqm}^*(\boldsymbol{x}), p_{eqm}^*(\boldsymbol{x}^*), \phi_{eqm}^*(\boldsymbol{x}^*))$ to the model at zero applied potential $V = 0$ and zero generation $j_{phot}^* \equiv 0$ for which the electric currents are identically zero everywhere $\boldsymbol{j}_n^* \equiv \boldsymbol{0}$ and $\boldsymbol{j}_p^* \equiv \boldsymbol{0}$. In particular, this requires that $R(n_{eqm}^*, p_{eqm}^*) \equiv 0$ along the entire

interface $\partial\Omega_i$. Such an equilibrium solution takes the form

$$n_{eqm}^* = n_+^* \exp\left(\frac{q}{kT}\left(\phi^* - \frac{V_{bi}}{2}\right)\right) \text{ in } \Omega_a, \quad p_{eqm}^* = p_- \exp\left(-\frac{q}{kT}\left(\phi^* + \frac{V_{bi}}{2}\right)\right) \text{ in } \Omega_d.$$

If the recombination $R(n^*, p^*)$ along the interface is to be zero, it is necessary that $np|_{\partial\Omega_i} = N_i^2$. Substitution of the above formulae for n_{eqm}^* and p_{eqm}^* into this yields the following relations between the parameters in the Ohmic boundary conditions (2.8) and (2.9) and the quantities N_i and V_{bi}:

$$n_- = N_i \Upsilon \exp\left(-\frac{qV_{bi}}{2kT}\right), \quad p_- = \frac{N_i}{\Upsilon}\exp\left(\frac{qV_{bi}}{2kT}\right), \quad n_+ = N_i \Upsilon \exp\left(\frac{qV_{bi}}{2kT}\right), \tag{2.20}$$
$$p_+ = \frac{N_i}{\Upsilon}\exp\left(-\frac{qV_{bi}}{2kT}\right),$$

for some dimensionless parameter Υ.

2.2 The non-dimensional model

Typical heterojunction devices are characterised by two lengthscales, namely the device lengthscale L and the micro-structure lengthscale, denoted by h. Motivated by the use of this device to generate current under illumination, we non-dimensionalise electron and hole current densities $\boldsymbol{j}_n^*$ and $\boldsymbol{j}_p^*$ with the typical photogenerated current. This is calculated by noting that the typical number of excitons generated per unit cross-sectional of the device (normal to the y-axis) is $Q_0\mathcal{A}_d L$; assuming that a significant number of these go on to generate electron–hole pairs that lead to an estimate of the photogenerated current density of $qQ_0\mathcal{A}_d L$. Assuming that a significant portion reaches the acceptor/donor interface and balancing the diffusive terms in (2.11)–(2.12) with the generation terms, over the micro-structure lengthscale h, leads to an estimate of the exciton number density c of $h^2 Q_0\mathcal{A}_d/\bar{\mathcal{D}}$ (where $\bar{\mathcal{D}}$ is a typical exciton diffusivity). On choosing to scale the electric potential with the thermal voltage kT/q and distances with the cell half-width L, we obtain the following scalings:

$$x^* = Lx, \quad t^* = \frac{L^2}{\bar{D}}t, \quad n^* = \frac{Q_0\mathcal{A}_d L^2}{\bar{D}}n, \quad p^* = \frac{Q_0\mathcal{A}_d L^2}{\bar{D}}p, \quad \Theta^* = \frac{\bar{D}^2 R_0}{Q_0^2 \mathcal{A}_d^2 L^4}\Theta,$$
$$\phi^* = \frac{kT}{q}\phi, \quad c_a^* = \frac{h^2 Q_0\mathcal{A}_d}{\bar{\mathcal{D}}}c_a, \quad c_d^* = \frac{h^2 Q_0\mathcal{A}_d}{\bar{\mathcal{D}}}c_d, \quad \boldsymbol{j}_n^* = qQ_0\mathcal{A}_d L\boldsymbol{j}_n, \tag{2.21}$$
$$\boldsymbol{j}_p^* = qQ_0\mathcal{A}_d L\boldsymbol{j}_p, \quad R^* = R_0 R, \quad Q^* = Q_0 Q, \quad j_{phot}^* = qQ_0\mathcal{A}_d h J_{phot}.$$

Substitution of the above scalings into (2.1)–(2.8) and (2.10)–(2.18), the model for a device with blocking layers (cf., Figure 1(c)) yields, on setting $\bar{\mathcal{D}} = (\mathcal{D}_a \mathcal{D}_d)^{1/2}$ and $\bar{D} = (D_n D_p)^{1/2}$

and enforcing the detailed balance relation (2.20), the dimensionless equations

$$
\left.
\begin{aligned}
\frac{\partial p}{\partial t} + \nabla \cdot \boldsymbol{j}_p &= 0 \\
\boldsymbol{j}_p &= -\kappa \left(\nabla p + p \nabla \phi \right) \\
\delta^2 v \frac{\partial c_d}{\partial t} &= \delta^2 \chi \nabla^2 c_d + Q(y) - \beta_d c_d
\end{aligned}
\right\} \quad \text{in} \quad \Omega_d, \quad (2.22)
$$

$$
\left.
\begin{aligned}
\frac{\partial n}{\partial t} - \nabla \cdot \boldsymbol{j}_n &= 0 \\
\boldsymbol{j}_n &= \frac{1}{\kappa} \left(\nabla n - n \nabla \phi \right) \\
\delta^2 v \frac{\partial c_a}{\partial t} &= \frac{\delta^2}{\chi} \nabla^2 c_a + G_a Q(y) - \beta_a c_a
\end{aligned}
\right\} \quad \text{in} \quad \Omega_a, \quad (2.23)
$$

$$
\nabla \cdot \left(\left(\mathcal{E} \mathcal{H}_d + \frac{1}{\mathcal{E}} (1 - \mathcal{H}_d) \right) \nabla \phi \right) = \frac{1}{\lambda^2} \left((1 - \mathcal{H}_d) n - \mathcal{H}_d p \right) \quad \text{in} \quad \Omega_d \cup \Omega_a, \quad (2.24)
$$

$$
\frac{\partial Q}{\partial y} = -\frac{K}{\cos \theta} \left((1 - F(y)) + G_a F(y) \right) Q \quad \text{in} \quad \Omega_d \cup \Omega_a, \quad (2.25)
$$

$$
\boldsymbol{j}_n \cdot \boldsymbol{N}|_{\partial \Omega_i} = \boldsymbol{j}_p \cdot \boldsymbol{N}|_{\partial \Omega_i} = \delta (\Gamma R(n,p) - J_{phot}), \ c_a|_{\partial \Omega_i} = 0, \ c_d|_{\partial \Omega_i} = 0, \quad (2.26)
$$

$$
\left.
\begin{aligned}
\phi &= \frac{\Phi - \Phi_{bi}}{2} \\
p &= \frac{\hat{n}}{\Upsilon} \\
Q &= \cos \theta \\
\frac{\partial c_d}{\partial y} &= 0
\end{aligned}
\right\} \quad \text{on} \ y = -1, \text{ and} \quad
\left.
\begin{aligned}
\phi &= -\frac{\Phi - \Phi_{bi}}{2} \\
n &= \hat{n} \Upsilon \\
\frac{\partial c_a}{\partial y} &= 0
\end{aligned}
\right\} \quad \text{on} \ y = 1. \quad (2.27)
$$

In the case of a device without blocking layers (cf., Figure 1(b)), substitution of the scalings (2.21) into (2.1)–(2.7) and (2.9)–(2.18) yields identical dimensionless equations with the exception that the boundary conditions on the electron and hole concentrations now read

$$
n|_{\{y=-1\} \cup \Omega_a} = \hat{n} \Upsilon e^{-\Phi_{bi}}, p|_{\{y=-1\} \cup \Omega_d} = \frac{\hat{n}}{\Upsilon}, n|_{\{y=1\} \cup \Omega_a} = \hat{n} \Upsilon, p|_{\{y=1\} \cup \Omega_d} = \frac{\hat{n}}{\Upsilon} e^{-\Phi_{bi}}. \quad (2.28)
$$

The interfacial recombination rate $R(n,p)$ and the characteristic function $\mathcal{H}_d$ are defined by

$$
R(n,p) = \Theta(n,p)(np - \hat{n}^2 e^{-\Phi_{bi}}) \quad (2.29)
$$

$$
\text{and} \quad \mathcal{H}_d = 1 \quad \text{in} \ \Omega_d \quad \text{and} \quad \mathcal{H}_d = 0 \quad \text{in} \ \Omega_a, \quad (2.30)
$$

and the interfacial photocurrent by

$$
J_{phot} = \delta \gamma_{eff} \left(\frac{1}{\chi} \nabla c_a \bigg|_{\partial \Omega_i} - \chi \nabla c_d \bigg|_{\partial \Omega_i} \right) \cdot \boldsymbol{N}. \quad (2.31)
$$

The dimensionless parameters are defined by

$$\hat{n} = \frac{N_i(D_n D_p)^{1/2}}{Q_0 \mathcal{A}_d L^2} e^{\Phi_{bi}/2}, \quad \kappa = \left(\frac{D_p}{D_n}\right)^{1/2}, \quad \Phi = \frac{q}{kT}V, \quad \Phi_{bi} = \frac{q}{kT}V_{bi},$$

$$\mathcal{E} = \left(\frac{\epsilon_d}{\epsilon_a}\right)^{1/2}, \quad v = \left(\frac{D_p D_n}{\mathcal{D}_a \mathcal{D}_d}\right)^{1/2}, \chi = \left(\frac{\mathcal{D}_d}{\mathcal{D}_a}\right)^{1/2}, \Gamma = \frac{R_0}{Q_0 \mathcal{A}_d h},$$

$$K = L\mathcal{A}_d, \quad \lambda = \frac{L_d}{L}, \quad \delta = \frac{h}{L},$$

$$\beta_a = \frac{\alpha_a h^2}{(\mathcal{D}_a \mathcal{D}_d)^{1/2}}, \beta_d = \frac{\alpha_d h^2}{(\mathcal{D}_a \mathcal{D}_d)^{1/2}}, G_a = \frac{\mathcal{A}_a}{\mathcal{A}_d},$$

where L_d is the Debye length defined (in terms of the typical charge density in the device, ρ_{typ}, arising from charge carrier generation) by

$$L_d = \left(\frac{(\epsilon_a \epsilon_d)^{1/2} kT}{q \rho_{typ}}\right)^{1/2} \quad \text{where} \quad \rho_{typ} = q \frac{Q_0 \mathcal{A}_d L^2}{(D_n D_p)^{1/2}}.$$

Henceforth, for simplicity of notation, we drop the *’s from the dimensionless variables.

2.2.1 *Parameter estimates*

We estimate the size of the dimensionless parameters in the model primarily on the basis of the work by Koster *et al.* [36] who consider a representative polymer/fullerene heterojunction device made from the organic semiconductors PPV and PCBM (Poly (p-phenylene vinylene) and Phenyl-C61-butyric acid methyl ester, respectively). The material parameters given therein are

$$\epsilon_a = 3 \times 10^{-11}\,\text{As}\,\text{V}^{-1}\,\text{m}^{-1}, \epsilon_d = 3 \times 10^{-11}\,\text{As}\,\text{V}^{-1}\,\text{m}^{-1}, D_n = 6.5 \times 10^{-9}\,\text{m}^2\,\text{s}^{-1},$$

$$D_p = 7.8 \times 10^{-10}\,\text{m}^2\,\text{s}^{-1}, V_{bi} = 1.34\,\text{V}, N_i \exp\left(\frac{qV_{bi}}{2kT}\right) = 2.5 \times 10^{25}\,\text{m}^{-3},$$

$$L = 120 \times 10^{-9}\,\text{m} \quad Q_0 \mathcal{A}_d = 5.4 \times 10^{27}\,\text{m}^{-3}\,\text{s}^{-1}.$$

Exciton diffusion lengths $(\mathcal{D}_d/\alpha_d)^{1/2}$ in PPV are around 5 nm [40], and although we have no direct information about h the size of the device micro-structure, we expect that, since it is able to convert most of the light it absorbs in reverse bias, h is smaller or comparable to 5 nm. We take $h = 3$ nm. In addition, the generation of excitons, via the absorption of light, is typically significantly higher in a polymeric donor material than in a fullerene acceptor (e.g., [53]) so that $G_a < 1$, although this depends strongly on the frequency of the incident radiation. In light of the above discussion, we make the following estimates of important parameters in the model:

$$\lambda = 0.1, \kappa \sim 0.35, \delta = 0.025, \Phi_{bi} = 50, \hat{n} \sim 720, \mathcal{E} = 1, \beta_d \sim 1, \beta_a \sim 1.$$

Furthermore, Koster *et al.* [36] asserts that the light absorption length is much greater than the width of the device, so that $K \ll 1$.

3 Numerical solution to the full model in an interdigitated device

In order to solve the dimensionless equations (2.22)–(2.31) over a region with an interdigitated interface, $\partial\Omega_i$ (such as that depicted in Figure 3), we use a finite element scheme based on a piecewise linear approximation to the solution. The full details of this scheme are outlined in Appendix B.

The main difficulty that arises in approximating the model numerically arises because p and n are defined only in the domains Ω_d and Ω_a, respectively, and are related solely by a condition along the common interface between these two domains $\partial\Omega_i$. In turn, this interface lies in the interior of the domain $\Omega_d \cup \Omega_a$ on which c and ϕ must be solved. The two main methods for tackling such problems are known as fitted and unfitted finite element methods. In the former the mesh is isoparametrically fitted to the interface $\partial\Omega_i$ whereas in the latter the mesh is independent of $\partial\Omega_i$; a detailed description of these methods is given in [4]. Here, we opt for a fitted finite element method and for simplicity we take our triangulated mesh, $\mathcal{T}^h$, of Ω to be such that the curve $\partial\Omega_i$ is approximated by a piecewise affine curve $\partial\Omega_i^h$ that is comprised of triangle edges so that each triangle of $\mathcal{T}^h$ lies either entirely in $\overline{\Omega}_d$ or $\overline{\Omega}_a$. A further difficulty that arises, in some parameter regimes, is the appearance of large gradients in the solution in the neighbourhood of the interface, and in order to deal with this we employ a non-uniform mesh.

The model (2.22)–(2.31) comprises of a system of strongly coupled partial differential equations; however, by using a semi-implicit backward Euler finite element approximation it can be reduced to an uncoupled system of linear equations, (B 7)–(B 11), for the approximate solutions c_h^k, ϕ_h^k, p_h^k and n_h^k. In order to obtain the solution at the k-th time step, from the data for p_h^{k-1}, n_h^{k-1} and c_h^{k-1} at the $k-1$-th time step, we first solve (B 7) and (B 8) for c_h^k, before solving (B 9) for ϕ_h^k and finally use these results (together with the data from the $k-1$-th time step) to solve (B 10) and (B 11) for p_h^k and n_h^k.

Numerical simulations of bilayer devices with sinusoidal interfaces have previously been presented in [9] and simulations for more realistic devices with complex active layer morphologies can be found in [35]. In [7], numerical examples showing the steady-state device behaviour, calculated from different applied potentials, of the organic photovoltaic bilayer devices are presented, whereas in [19] the authors apply Rothe's method, which is an advanced time-step control technique, to accurately estimate photocurrent transient times. The software package WIAS-TeSCA [23] has very efficient numerical procedures for solving two- and three-dimensional finite element approximations of drift-diffusion and photovoltaic models; the main ideas of these procedures are given in [22]. In [2], three-dimensional simulations, using WIAS-TeSCA, of a thin film heterojunction solar cell with a point contact/defect passivation structure at the heterointerface are presented.

3.1 The geometry

In order to illustrate the nature of the solutions in a typical micro-structured geometry we solve in the domain Ω between contacts at $y = -1$ and $y = 1$ and with a 2δ-periodic interface $\partial\Omega_i$, separating the acceptor and donor regions (Ω_a and Ω_d, respectively), given by the curve $y = 0.7\cos(\pi\delta x)$, see Figure 3.

3.2 Results

In all the simulations we present, we consider a Langevin recombination along $\partial\Omega_i$, e.g., [8, 36], of the form

$$R(n, p) = np \qquad (3.1)$$

in which we neglect the thermal generation term $-\hat{n}^2 e^{-\Phi_{bi}}$ because it is, in physically realistic regimes, vanishingly small. We choose the other parameters in the problem to be given by, what we believe to be, physically realistic values:

$$\delta = 0.025, \ \lambda = 0.4, \ \kappa = 0.35, \ \hat{n} \sim 750, \ \mathcal{E} = 1, \ \beta_d = 1, \ \beta_a = 1, \ K = 0.1,$$
$$\Gamma = 2 \times 10^{-8}, \ \gamma_{eff} = 0.75, \ G_a = 0.3, \ v = 1, \ \chi = 1, \ \delta = 0.025, \ \Upsilon = 1, \qquad (3.2)$$

and we took the incident radiation to be normal to the cell so that $\theta = 0$. On noting that the solution depends only on the dimensionless applied bias Φ and built-in voltage through their difference $\Phi - \Phi_{bi}$, we choose to illustrate the nature of the solution by looking at three values of this quantity, namely $\Phi - \Phi_{bi} = -6$, $\Phi - \Phi_{bi} = 0$ and $\Phi - \Phi_{bi} = 3$, representing regimes in which the applied potential is held below, at, and above the built-in voltage, respectively. The results of three simulations are shown in Figure 2, where, for ease of visibility, the domain Ω has been rescaled so that its length is the same size as its height. Here, contour plots of the stationary solution for p (left hand), n (centre) and ϕ (right hand) are presented, with $\Phi - \Phi_{bi} = -6$ (upper), $\Phi - \Phi_{bi} = 0$ (centre) and $\Phi - \Phi_{bi} = 3$ (lower). It is notable that for $\Phi - \Phi_{bi} = -6$, the solution is almost entirely independent of x, i.e., it does not 'see' the fine details of the micro-structure. In fact this is a characteristic feature of all solutions for which $\Phi < \Phi_{bi}$, and indeed it can be seen that even for $\Phi = \Phi_{bi}$ the dependence of the solution on x is relatively weak. However, this feature of the solution changes rapidly as Φ increases above the built in voltage; thus, we see, where $\Phi - \Phi_{bi} = 3$, the development of boundary layers about the interface ($\partial\Omega_i$) between the acceptor and donor, even though in dimensional terms of the applied potential, has only exceeded the built-in voltage by 3 thermal voltages (corresponding to 0.075 V at room temperature).

4 Derivation of the homogenised equations as $\delta \to 0$

A noteworthy feature of the numerical solution to the (full) model of the bulk heterojunction is that, for applied potentials Φ less than the built-in voltage Φ_{bi}, the solution does not change significantly over the dimensions of the micro-structure, and so for the interdigitated morphology that we considered in Section 3.2, the solution is almost entirely independent of the spatial variable x. This suggests that, at least in the regime $\Phi < \Phi_{bi}$, it is appropriate to use the method of homogenisation to derive effective medium equations for the device. Since the regime $\Phi < \Phi_{bi}$ typically corresponds to the power generating regime of the device, the resulting effective medium equations can be used to accurately characterise its electrical behaviour relevant to its use as a solar cell. Considerable savings in numerical time and effort can be obtained by using effective medium equations in place of the full model (which, as discussed in Section 3.2, is hard to solve). Furthermore, use of effective medium equations, in which an intricate micro-structure is replaced by
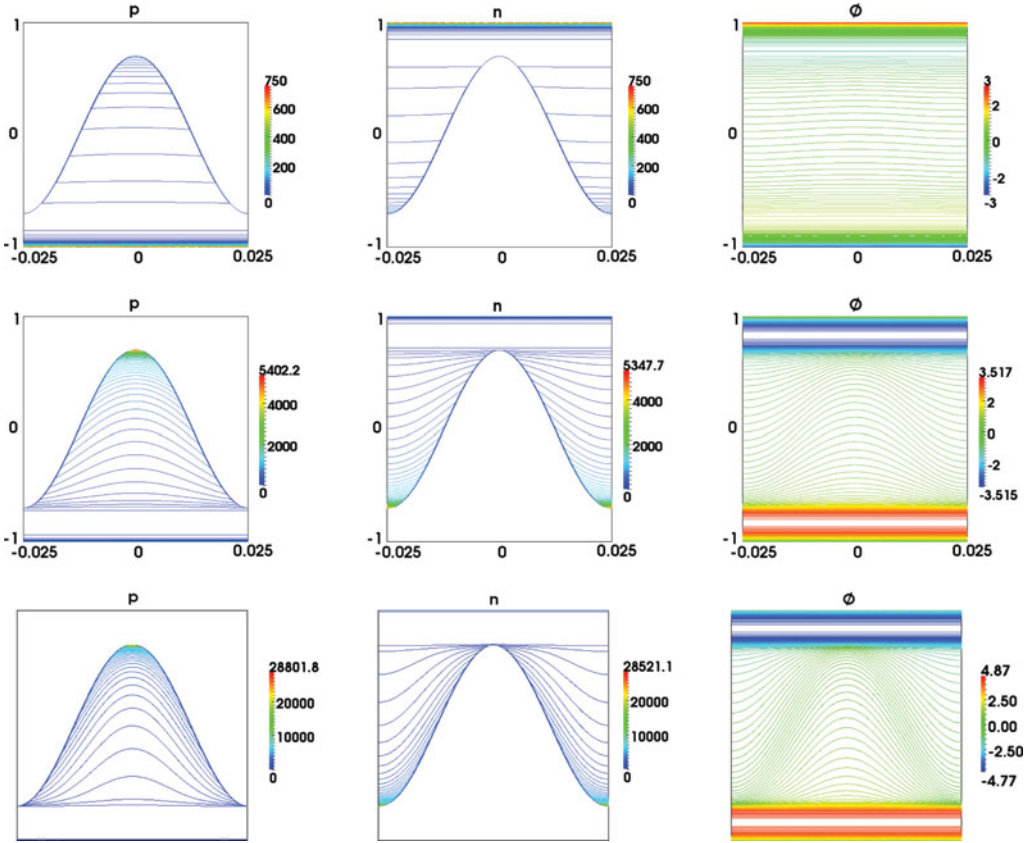
FIGURE 2. Stationary solutions of the full dimensionless model, with parameter values given in (3.2), p_h, (left), n_h, (centre), ϕ_h, (right) for $\Phi - \Phi_{bi} = -6$ (upper), $\Phi - \Phi_{bi} = 0$ (middle), $\Phi - \Phi_{bi} = 3$ (lower).

functions representing averaged features of this micro-structure, has the advantage that it allows device behaviour to be understood in terms of the gross (averaged) micro-structural features.

Here, we consider the derivation of homogenised equations from the non-dimensional model (given in (2.22)–(2.31) based upon the disparity between the scale of the device micro-structure h and its width L; formally, we take the limit $\delta = h/L \rightarrow 0$. We treat two separate scenarios, one in which the device has an interdigitated structure (as depicted later in Figure 3) and the other in which the device has a locally periodic three-dimensional structure (such as that depicted later in Figure 6). These two scenarios are described in Sections 4.1 and 4.2. The first of these scenarios is considerably easier to treat mathematically and is so described in detail in the main text, whereas the details of the derivation for the locally periodic structure (whilst more pertinent to bulk heterojunctions) are relegated to Appendix A. In both cases, however, the homogenised equations have the same form. Comparison between the results of the homogenised model
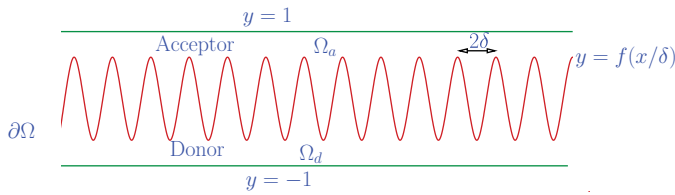
FIGURE 3. The geometry of the cell.

derived in Section 4.1 and the full non-dimensional equations (2.22)–(2.31) is then made in Section 3.

4.1 Homogenisation for an interdigitated device

4.1.1 *The geometry of the device*

Consider a device with a two-dimensional, highly convoluted, interdigitated interface between the two semiconductors that is given by the periodic curve

$$y = f(\xi), \qquad \text{where} \qquad x = \delta \xi \qquad \text{and} \qquad f \text{ is a two-periodic even function.}$$

The problem can then be considered on a periodic subdomain, as shown in Figure 4, with suitable periodic conditions on the left and right boundaries. Here, it is helpful to express this curve in terms of its inverse $\xi = 1 - F(y)$, where $y \in (\alpha, \beta)$ and ξ ranges between 0 and 1 (see Figure 4). Note that $F(y)$ can, as in equation (2.25), be identified as the volume fraction of the acceptor material at depth y. With this definition of the interface in $0 < \xi < 1$, the unit normal to the interface can be expressed in the form

$$N = \frac{\nabla(\xi - (1 - F(y)))}{|\nabla(\xi - (1 - F(y)))|} = \frac{e_x + \delta F'(y)e_y}{\sqrt{1 + \delta^2 F'(y)^2}}, \tag{4.1}$$

where e_x and e_y are unit vectors in the direction of positive x and y, respectively, and a prime denotes a derivative with respect to y. In (4.1), the gradient operator is considered with respect to x and y, and in terms of the variables ξ and y, it takes the form

$$\nabla = \frac{e_x}{\delta} \frac{\partial}{\partial \xi} + e_y \frac{\partial}{\partial y}.$$

4.1.2 *Homogenised equations from the two-dimensional model*

We homogenise over the micro-structure of the device in the region $\alpha < y < \beta$, where acceptor and donor materials interpenetrate (see Figure 4). We follow standard procedure and assume that the micro-structure lengthscale $\delta \ll 1$ and that the function $(\Gamma R(n, p) - J_{phot})$ and parameters λ, Φ, Φ_{bi}, $\mathcal{E}$, K, β_a, β_d, v, κ and χ are all formally $O(1)$.
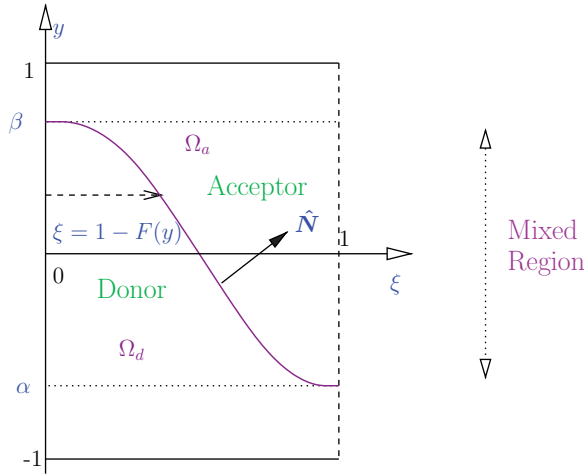
FIGURE 4. A schematic of the subdomain over which the model is solved.

Asymptotic expansion

We write $\boldsymbol{j}_n = u_n \boldsymbol{e}_x + v_n \boldsymbol{e}_y$ and $\boldsymbol{j}_p = u_p \boldsymbol{e}_x + v_p \boldsymbol{e}_y$ and expand as follows:

$$n = n_0(y,t) + \delta^2 n_2(\xi,y,t) + \cdots, \quad p = p_0(y,t) + \delta^2 p_2(\xi,y,t) + \cdots,$$
$$\phi = \phi_0(y,t) + \delta^2 \phi_1(\xi,y,t) + \cdots, \quad J_{phot} = J_{phot,0} + \cdots,$$
$$c_d = c_{d,0}(\xi,y,t) + \cdots, \quad c_a = c_{a,0}(\xi,y,t) + \cdots,$$
$$u_n = \delta u_{n,1}(\xi,y,t) + \cdots, \quad v_n = v_{n,0}(y,t) + \cdots,$$
$$u_p = \delta u_{p,1}(\xi,y,t) + \cdots, \quad v_p = v_{p,0}(y,t) + \cdots.$$

On substitution into (2.23)–(2.24), this yields, to leading order in the region $\alpha < y < \beta$,

$$\frac{\partial n_0}{\partial t} - \frac{\partial u_{n,1}}{\partial \xi} - \frac{\partial v_{n,0}}{\partial y} = 0 \qquad \text{for} \quad 1 - F(y) < \xi < 1, \tag{4.2}$$

$$\frac{\partial p_0}{\partial t} + \frac{\partial u_{p,1}}{\partial \xi} + \frac{\partial v_{p,0}}{\partial y} = 0 \qquad \text{for} \quad 0 < \xi < 1 - F(y), \tag{4.3}$$

$$v_{n,0} = \kappa_n \left(\frac{\partial n_0}{\partial y} - n_0 \frac{\partial \phi_0}{\partial y} \right) \qquad \text{for} \quad 1 - F(y) < \xi < 1, \tag{4.4}$$

$$v_{p,0} = -\kappa_p \left(\frac{\partial p_0}{\partial y} + p_0 \frac{\partial \phi_0}{\partial y} \right) \qquad \text{for} \quad 0 < \xi < 1 - F(y), \tag{4.5}$$

$$\frac{\partial}{\partial \xi} \left((\frac{1}{\mathcal{E}} H(\xi - 1 + F(y)) + \mathcal{E} H(1 - F(y) - \xi)) \frac{\partial \phi_1}{\partial \xi} \right)$$
$$+ \frac{\partial}{\partial y} \left((\frac{1}{\mathcal{E}} H(\xi - 1 + F(y)) + \mathcal{E} H(1 - F(y) - \xi)) \frac{\partial \phi_0}{\partial y} \right)$$
$$= \frac{1}{\lambda^2} \left(H(\xi - 1 + F(y)) n_0 - H(1 - F(y) - \xi) p_0 \right), \tag{4.6}$$

$$\chi \frac{\partial^2 c_{d,0}}{\partial \xi^2} + Q(y) - \beta_d c_{d,0} = 0, \qquad \text{for} \quad 0 < \xi < 1 - F(y), \tag{4.7}$$

$$\frac{1}{\chi} \frac{\partial^2 c_{a,0}}{\partial \xi^2} + G_a Q(y) - \beta_a c_{a,0} = 0, \qquad \text{for} \quad 1 - F(y) < \xi < 1, \tag{4.8}$$

$$J_{phot,0} = \gamma_{eff} \left(\frac{1}{\chi} \frac{\partial c_{a,0}}{\partial \xi} \bigg|_{\xi=(1-F(y))^+} - \chi \frac{\partial c_{d,0}}{\partial \xi} \bigg|_{\xi=(1-F(y))^-} \right). \tag{4.9}$$

The symmetry of the problem and the interface conditions (2.26)–(2.27) give

$$\begin{aligned}
\frac{\partial n_2}{\partial \xi} \bigg|_{\xi=1} &= 0, \; u_{n,1}|_{\xi=1} = 0, \; \frac{\partial \phi_1}{\partial \xi} \bigg|_{\xi=1} = 0, \\
\frac{\partial p_2}{\partial \xi} \bigg|_{\xi=0} &= 0, \; u_{p,1}|_{\xi=0} = 0, \; \frac{\partial \phi_1}{\partial \xi} \bigg|_{\xi=0} = 0,
\end{aligned} \tag{4.10}$$

$$\frac{\partial c_{d,0}}{\partial \xi} \bigg|_{\xi=0} = 0, \; c_{d,0}|_{\xi=1-F(y)} = 0, \; c_{a,0}|_{\xi=1-F(y)} = 0, \; \frac{\partial c_{a,0}}{\partial \xi} \bigg|_{\xi=1} = 0, \tag{4.11}$$

$$\left(u_{n,1} + F'(y) v_{n,0} \right) \big|_{\xi=1-F(y)} = \Gamma R(n_0, p_0) - J_{phot}|_{\xi=1-F(y)}, \tag{4.12}$$

$$\left(u_{p,1} + F'(y) v_{p,0} \right) \big|_{\xi=1-F(y)} = \Gamma R(n_0, p_0) - J_{phot}|_{\xi=1-F(y)}. \tag{4.13}$$

Integrating (4.2) with respect to ξ between $\xi = 1 - F(y)$ and 1 yields

$$F(y) \frac{\partial n_0}{\partial t} - [u_{n,1}]^1_{\xi=1-F(y)} - F(y) \frac{\partial v_{n,0}}{\partial y} = 0.$$

Applying the boundary conditions (4.10a), (4.10b), and (4.12) leads to an equation for $n_0(y, t)$:

$$F(y) \frac{\partial n_0}{\partial t} - \frac{\partial}{\partial y} \left(F(y) v_{n,0} \right) = J_{phot} - \Gamma R(n_0, p_0) \text{ in } \alpha \leqslant y \leqslant \beta. \tag{4.14}$$

A similar equation can be derived for $p_0(y, t)$ by integrating (4.3) with respect to ξ between $\xi = 0$ and $1 - F(y)$; and applying the boundary conditions (4.10d), (4.10e), and (4.13) to the result. This results in the following:

$$(1 - F(y)) \frac{\partial p_0}{\partial t} + \frac{\partial}{\partial y} \left((1 - F(y)) v_{p,0} \right) = J_{phot} - \Gamma R(n_0, p_0) \text{ in } \alpha \leqslant y \leqslant \beta. \tag{4.15}$$

The equation for $\phi_0(y, t)$ can be derived by a similar procedure, namely integrating (4.5) between $\xi = 0$ and 1 and applying the symmetry conditions (4.10c) and (4.10f) to the result. This yields

$$\frac{\partial}{\partial y} \left((\frac{1}{\mathcal{E}} F(y) + \mathcal{E}(1 - F(y))) \frac{\partial \phi_0}{\partial y} \right) = \frac{1}{\lambda^2} (F(y) n_0 - (1 - F(y)) p_0) \text{ in } \alpha \leqslant y \leqslant \beta. \tag{4.16}$$

The three homogenised equations (4.14)–(4.16) for the five quantities $n_0(y,t)$, $p_0(y,t)$, $\phi_0(y,t)$, $v_{n,0}(y,t)$, and $v_{p,0}(y,t)$ couple to the two equations (4.4) and (4.5) to form a closed system.

Finally, we can derive an expression for $J_{phot,0}$ by solving (4.8) and (4.7) with boundary conditions (4.11) to obtain

$$c_{d,0} = \frac{Q(y)}{\beta_d} \left(1 - \frac{\cosh\left((\beta_d/\chi)^{1/2} \xi \right)}{\cosh\left((\beta_d/\chi)^{1/2} (1 - F(y)) \right)} \right) \quad \text{on} \quad 0 < \xi < 1 - F(y), \quad (4.17)$$

$$c_{a,0} = \frac{G_a Q(y)}{\beta_a} \left(1 - \frac{\cosh\left((\beta_a \chi)^{1/2} (1 - \xi) \right)}{\cosh\left((\beta_a \chi)^{1/2} F(y) \right)} \right) \quad \text{on} \quad 1 - F(y) < \xi < 1, \quad (4.18)$$

which leads, on substitution into (4.7), to the following formula for $J_{phot,0}$ in $\alpha \leqslant y \leqslant \beta$:

$$J_{phot,0} = \gamma_{eff} Q(y) \left(\frac{G_a}{(\beta_a \chi)^{1/2}} \tanh\left((\beta_a \chi)^{1/2} F(y) \right) + \left(\frac{\chi}{\beta_d} \right)^{1/2} \tanh\left(\left(\frac{\beta_d}{\chi} \right)^{1/2} (1 - F(y)) \right) \right). \tag{4.19}$$

Since there is no interface on which excitons can dissociate in $-1 < y < \alpha$ and $\beta < y < 1$, it follows that $J_{phot,0}(y) = 0$ for y in these ranges. Furthermore, it is unsurprising that the homogenised variable $J_{phot,0}$ is discontinuous at $y = \alpha$ and $y = \beta$ because at these two positions there is sharp discontinuity in the length of interface (per unit width of cell). In addition, the intensity function $Q(y)$ is obtained by direct integration of (2.25) with the boundary condition $Q|_{y=-1} = \cos\theta$.

Summary of the homogenised model

The homogenisation of the interdigitated geometry described in Section 4.1.1 leads to an approximate, one-dimensional model given by equations (4.14)–(4.16) and (4.19) for n, p, and ϕ and the electron and hole currents, j_n and j_p. On dropping subscripts, and extending the validity of the equations into the blocking layers ($-1 < y < \alpha$ and $\beta < y < 1$), the homogenised equations can be written in the form

$$\left. \begin{aligned} (1 - F(y))\frac{\partial p}{\partial t} + \frac{\partial J_p}{\partial y} &= \left(J_{phot} - \Gamma R(n,p) \right) H(y - \alpha) \\ J_p &= -\kappa(1 - F(y)) \left(\frac{\partial p}{\partial y} + p\frac{\partial \phi}{\partial y} \right) \end{aligned} \right\} \quad \text{in} \quad -1 < y < \beta, \quad (4.20)$$

$$\left. \begin{aligned} F(y)\frac{\partial n}{\partial t} - \frac{\partial J_n}{\partial y} &= \left(J_{phot} - \Gamma R(n,p) \right) H(\beta - y) \\ J_n &= \frac{F(y)}{\kappa} \left(\frac{\partial n}{\partial y} - n\frac{\partial \phi}{\partial y} \right) \end{aligned} \right\} \quad \text{in} \quad \alpha < y < 1, \quad (4.21)$$

$$\frac{\partial}{\partial y} \left(\left(\frac{1}{\mathcal{E}} F(y) + \mathcal{E}(1 - F(y)) \right) \frac{\partial \phi}{\partial y} \right) = \frac{1}{\lambda^2} \left(nF(y) - p(1 - F(y)) \right) \quad \text{in} \quad -1 < y < 1, \quad (4.22)$$

where we denote current densities averaged across the device cross-section by $J_p = (1 - F(y))j_p$ and $J_n = F(y)j_n$ and where

$$J_{phot} = \gamma_{eff} Q(y) \left(\frac{G_a}{(\beta_a \chi)^{1/2}} \tanh \left((\beta_a \chi)^{1/2} F(y) \right) + \left(\frac{\chi}{\beta_d} \right)^{1/2} \tanh \left(\left(\frac{\beta_d}{\chi} \right)^{1/2} (1 - F(y)) \right) \right)$$

(4.23)

valid in $\alpha < y < \beta$, and

$$Q(y) = \cos(\theta) \exp \left(-\frac{K}{\cos \theta} \int_{-1}^{y} (1 - F(z)(1 - G_a)) dz \right).$$

(4.24)

The boundary conditions, for a device with finite blocking layers, are

$$\left. \begin{array}{c} \phi = \dfrac{\Phi - \Phi_{bi}}{2} \\[2mm] p = \dfrac{\hat{n}}{\Upsilon} \end{array} \right\} \quad \text{on} \ \ y = -1, \qquad \left. \begin{array}{c} \phi = -\dfrac{\Phi - \Phi_{bi}}{2} \\[2mm] n = \hat{n}\Upsilon \end{array} \right\} \quad \text{on} \ \ y = 1, \qquad (4.25)$$

$$J_n \to 0 \quad \text{as} \ \ y \searrow \alpha, \qquad J_p \to 0 \quad \text{as} \ \ y \nearrow \beta; \qquad (4.26)$$

these are illustrated in Figure 5(c). In the case of a device without blocking layers (i.e., one for which $F(-1) > 0$ and $F(1) < 1$), the zero electron and hole current conditions on $y = \alpha$ and $y = \beta$ (i.e., (4.26)) are replaced by the following Ohmic boundary conditions on $y = \pm 1$:

$$n|_{y=-1} = \hat{n}\Upsilon e^{-\Phi_{bi}} \quad \text{and} \quad p|_{y=1} = \frac{\hat{n}}{\Upsilon} e^{-\Phi_{bi}}; \qquad (4.27)$$

this case is illustrated in Figure 5(b).

4.1.3 *An alternative formulation of the homogenised model*

In order to solve the homogenised model (4.20)–(4.22) numerically, it is helpful to reformulate it in terms of Slotboom variables $A(y, t)$ and $B(y, t)$ by writing $n = A(y, t) \exp(\phi(y, t))$ and $p = B(y, t) \exp(-\phi(y, t))$. This results to the following formulation:

$$\left. \begin{array}{c} (1 - F(y)) \dfrac{\partial B e^{-\phi}}{\partial t} + \dfrac{\partial J_p}{\partial y} = \left(J_{phot} - \Gamma R(n, p) \right) H(y - \alpha) \\[3mm] \dfrac{\partial B}{\partial y} = -e^{\phi} \dfrac{J_p}{(1 - F(y))\kappa} \end{array} \right\} \quad \text{in} \ -1 < y < \beta, \qquad (4.28)$$

$$\left. \begin{array}{c} F(y) \dfrac{\partial A e^{\phi}}{\partial t} - \dfrac{\partial J_n}{\partial y} = \left(J_{phot} - \Gamma R(n, p) \right) H(\beta - y), \\[3mm] \dfrac{\partial A}{\partial y} = e^{-\phi} \dfrac{J_n \kappa}{F(y)} \end{array} \right\} \quad \text{in} \ \alpha < y < 1, \qquad (4.29)$$

$$\frac{\partial}{\partial y} \left(\left(\frac{1}{\mathcal{E}} F(y) + \mathcal{E}(1 - F(y)) \right) \frac{\partial \phi}{\partial y} \right) = \frac{1}{\lambda^2} \left(A e^{\phi} F(y) - B e^{-\phi}(1 - F(y)) \right) \quad \text{in} \ -1 < y < 1,$$
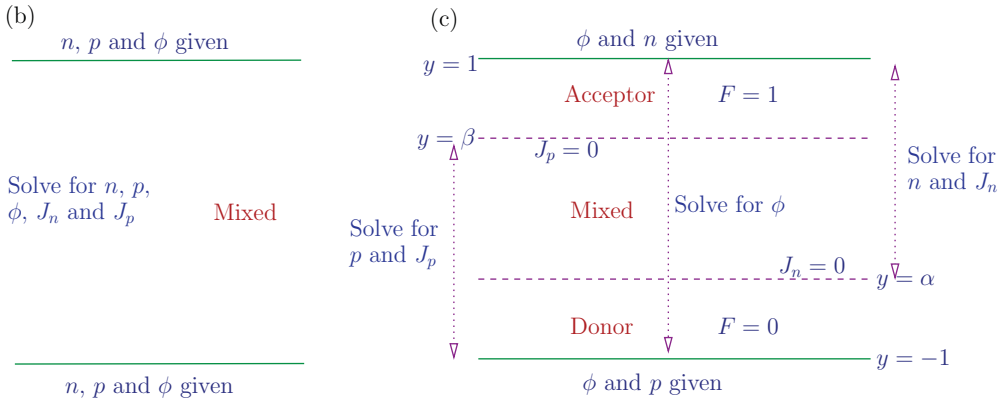
(4.30)

FIGURE 5. Boundary conditions on the homogenised model for the device geometries illustrated in Figures 1(b) and (c). Case (b) shows a bulk heterojunction without capping layers. Case (c) shows a bulk heterojunction with capping layers on pure donor and acceptor materials at the electrodes.

with J_{phot} given by (4.26) and the boundary conditions (for a device with blocking layers) are

$$
\left.\begin{array}{l}
\phi = \dfrac{\Phi - \Phi_{bi}}{2} \\[2mm]
B = \dfrac{\hat{n}}{\Upsilon} e^{\frac{\Phi - \Phi_{bi}}{2}}
\end{array}\right\} \quad \text{on} \quad y = -1, \qquad
\left.\begin{array}{l}
\phi = -\dfrac{(\Phi - \Phi_{bi})}{2} \\[2mm]
A = \hat{n}\Upsilon e^{\frac{(\Phi - \Phi_{bi})}{2}}
\end{array}\right\} \quad \text{on} \quad y = 1, \qquad (4.31)
$$

$$
J_n \to 0 \quad \text{as} \quad y \searrow \alpha, \qquad J_p \to 0 \quad \text{as} \quad y \nearrow \beta, \qquad (4.32)
$$

and in the case of a device without blocking layers the conditions (4.32) are replaced by

$$
A|_{y=-1} = \hat{n}\Upsilon e^{-\frac{(\Phi+\Phi_{bi})}{2}} \quad \text{and} \quad B|_{y=1} = \frac{\hat{n}}{\Upsilon} e^{-\frac{(\Phi+\Phi_{bi})}{2}}. \qquad (4.33)
$$

Notably the steady-state solutions to (4.28a) and (4.29a), in the restricted domains $-1 < y < \beta$ and $\alpha < y < 1$ (respectively), with internal boundary conditions (4.32) are equivalent to the solutions to (4.28a) and (4.29a) on the full domain $-1 < y < 1$, where the right-hand side of these equations is replaced by $\left(J_{phot} - \Gamma R(n,p)\right)(H(y-\alpha) - H(y-\beta))$ and where the boundary conditions (4.32) are replaced by $J_n|_{y=-1} = 0$ and $J_p|_{y=1} = 0$. It is this reformulation of (4.28)–(4.32) as a two point boundary value problem that we solve numerically.

4.2 A bulk heterojunction with three-dimensional micro-structure

Here, we consider how to derive homogenised equations for a bulk heterojunction with a fully three-dimensional (and almost periodic) micro-structure, such as occurs in spin-coated devices (e.g., [41]). The techniques required to perform this homogenisation are considerably more complex that those described for the interdigitated device in Section 4.1 and involve application of the formal asymptotic method of multiple scales as originally developed by Keller [30, 31] (relevant extensions of this method to applications in which the micro-structure is not entirely periodic are given in [6, 11, 48, 49]). We note further
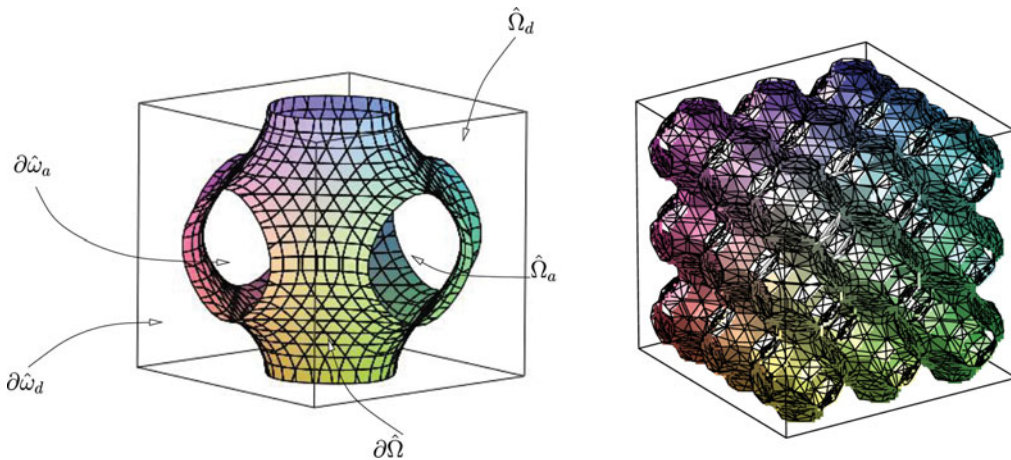
FIGURE 6. Left-hand panel: an illustration of the micro-structure geometry within one of the periodic boxes $\hat{V}$. Right-hand panel: repeated periodic boxes form the global micro-structure.

that there is an extensive literature on rigorous homogenisation methods (see [1, 14]) but that these methods involve considerably more effort than their formal counterparts whilst yielding exactly the same homogenised equations (they are also particularly hard to apply to micro-structures that are not strictly periodic). Here, we operate on the dimensionless equations (2.22)–(2.31) in which the device lengthscale is of $O(1)$ and that of the micro-structure is $O(\delta)$, where $\delta \ll 1$. Furthermore, we assume that the micro-structure is *locally* periodic inside a *globally* periodic array of boxes, which we denote by $\hat{\Omega}_d \cup \hat{\Omega}_a$. This approach allows us to consider geometries in which important features of the micro-structure (such as the donor volume fraction) are periodic on the lengthscale of the micro-structure but vary slowly over the device lengthscale (further discussion of the applicability of this technique are given in [50]). Consider now one of these boxes $\hat{V}$, say, whose volume is split into a part $\hat{\Omega}_d$ occupied by the donor material and a part $\hat{\Omega}_a$ occupied by the acceptor (see Figure 6 for an example configuration). Furthermore, we denote that part of the boundary to $\hat{\Omega}_a$ lying along the boundary of $\hat{V}$ by $\partial\hat{\omega}_a$ and that part lying along the interface between $\hat{\Omega}_a$ and $\hat{\Omega}_d$ by $\partial\hat{\Omega}$. Similarly, we denote that part of the boundary to $\hat{\Omega}_d$ lying along the boundary of $\hat{V}$ by $\partial\hat{\omega}_d$ and that part lying along the interface between $\hat{\Omega}_a$ and $\hat{\Omega}_d$ by $\partial\hat{\Omega}$. For the sake of generality we allow the micro-structure to change slowly, over the $O(1)$ lengthscale, and it is in this sense that it is *locally* periodic.

4.3 A multiple scales formulation of the problem.

We formally consider the distinguished limit in which κ, v, χ, β_d, β_a, G_a, $\mathcal{E}$, λ, Γ, and γ_{eff} are all $O(1)$ while $\delta \to 0$ and introduce the microscale variable $\hat{x}$ defined by

$$\boldsymbol{x} = \delta\hat{\boldsymbol{x}}.$$

We look for a solution to the problem (2.22)–(2.31) that is a function both of the microscale variable $\hat{x}$ and the device scale variable x. As is standard in such multiple scales calculations we look for a solution that is periodic in the microscale variable and transforms the gradient operator via $\nabla \rightarrow \nabla + \hat{\nabla}/\delta$. The central ansatz of the homogenisation is contained in the asymptotic expansion:

$$
\begin{aligned}
n &= n_0(x,t) + \delta n_1(x,\hat{x},t) + \delta^2 n_2(x,\hat{x},t) + \cdots, \\
p &= p_0(x,t) + \delta p_1(x,\hat{x},t) + \delta^2 p_2(x,\hat{x},t) + \cdots, \\
\phi &= \phi_0(x,t) + \delta \phi_1(x,\hat{x},t) + \delta^2 \phi_2(x,\hat{x}\,t) + \cdots, \\
c &= c_{d,0}(x,\hat{x},t) + \delta c_{d,1}(x,\hat{x},t) + \delta^2 c_{d,2}(x,\hat{x},t) + \cdots, \\
c &= c_{a,0}(x,\hat{x},t) + \delta c_{a,1}(x,\hat{x},t) + \delta^2 c_{a,2}(x,\hat{x},t) + \cdots, \\
\boldsymbol{j}_n &= \boldsymbol{j}_{n,0}(x,\hat{x},t) + \delta \boldsymbol{j}_{n,1}(x,\hat{x},t) + \delta^2 \boldsymbol{j}_{n,2}(x,\hat{x},t) + \cdots, \\
\boldsymbol{j}_p &= \boldsymbol{j}_{p,0}(x,\hat{x},t) + \delta \boldsymbol{j}_{p,1}(x,\hat{x},t) + \delta^2 \boldsymbol{j}_{p,2}(x,\hat{x},t) + \cdots, \\
J_{phot} &= J_{phot,0}(x,\hat{x},t) + \delta J_{phot,1}(x,\hat{x},t) + \delta^2 J_{phot,2}(x,\hat{x},t) + \cdots.
\end{aligned}
\tag{4.34}
$$

Thus, the electric potential and the concentrations of free electrons, holes, and excitons are all functions of the device lengthscale only at leading order. The electron and hole current densities both have to flow around the micro-structure and are thus functions of both device-scale and microscale variables at leading order.

4.3.1 *Summary of the homogenised equations*

The multiple scale analysis, the details of which are relegated to Appendix A, results in homogenised equations for the electron and hole concentrations (n and p, respectively), the electric potential ϕ, the volume averaged electron and hole current densities ($\langle \boldsymbol{j}_n \rangle$ and $\langle \boldsymbol{j}_p \rangle$, respectively) and the volume averaged electric displacement and photogeneration ($\langle \mathcal{D} \rangle$ and $\langle J_{phot} \rangle$, respectively). On dropping the 0 subscript from the leading order terms in the multiple scales expansion, these equations take the form

$$
(1 - F(x))\frac{\partial p}{\partial t} + \nabla \cdot \langle \boldsymbol{j}_p \rangle + b_{et}(x)(\Gamma R(n,p) - \langle J_{phot} \rangle) = 0,
\tag{4.35}
$$

$$
F(x)\frac{\partial n}{\partial t} - \nabla \cdot \langle \boldsymbol{j}_n \rangle + b_{et}(x)(\Gamma R(n,p) - \langle J_{phot} \rangle) = 0,
\tag{4.36}
$$

$$
\langle \boldsymbol{j}_p \rangle_i = -B_{ij}(x)\left(\frac{\partial p}{\partial x_j} + p\frac{\partial \phi}{\partial x_j}\right), \qquad \langle \boldsymbol{j}_n \rangle_i = C_{ij}(x)\left(\frac{\partial n}{\partial x_j} - n\frac{\partial \phi}{\partial x_j}\right),
\tag{4.37}
$$

$$
\nabla \cdot \langle \mathcal{D} \rangle = \frac{1}{\lambda^2}\left((1 - F(x))p(x,t) - F(x)n(x,t)\right), \text{where} \quad \langle \mathcal{D} \rangle = -A_{ij}(x)\frac{\partial \phi}{\partial x_j}e_i.
\tag{4.38}
$$

Here, $B_{ij}(x)$ and $C_{ij}(x)$ are the (dimensionless) electron and hole current conductivity tensors, $A_{ij}(x)$ is the (dimensionless) permittivity tensor, and $b_{et}(x)$ a (dimensionless)

measure of the surface area of interface per unit volume of material, defined by

$$B_{ij}(\boldsymbol{x}) = \frac{\kappa}{|\hat{\Omega}_d| + |\hat{\Omega}_a|} \int_{\hat{\Omega}_d} \left(\delta_{ij} - \frac{\partial \zeta^{(j)}}{\partial \hat{x}_i} \right) d\hat{V}, \tag{4.39}$$

$$C_{ij}(\boldsymbol{x}) = \frac{1}{\kappa(|\hat{\Omega}_d| + |\hat{\Omega}_a|)} \int_{\hat{\Omega}_a} \left(\delta_{ij} - \frac{\partial \eta^{(j)}}{\partial \hat{x}_i} \right) d\hat{V}, \tag{4.40}$$

$$A_{ij}(\boldsymbol{x}) = \frac{1}{|\hat{\Omega}_a| + |\hat{\Omega}_d|} \int_{\hat{\Omega}_a \cup \hat{\Omega}_d} \left(\mathcal{E}\mathcal{H}_d + \frac{1}{\mathcal{E}}(1 - \mathcal{H}_d) \right) \left(\delta_{ij} - (1 - \mathcal{E}^2)\frac{\partial \mu^{(j)}}{\partial \hat{x}_i} \right) d\hat{V}, \tag{4.41}$$

$$b_{et}(\boldsymbol{x}) = \frac{1}{|\hat{V}|} \int_{\partial \hat{\Omega}} d\hat{S}. \tag{4.42}$$

These tensor quantities depend on the micro-structure geometry through the nine characteristic functions $\mu^{(j)}(\boldsymbol{x}, \hat{\boldsymbol{x}})$, $\zeta^{(j)}(\boldsymbol{x}, \hat{\boldsymbol{x}})$, and $\eta^{(j)}(\boldsymbol{x}, \hat{\boldsymbol{x}})$ (for $j = 1, 2, 3$) which must be found by solving cell problems (A 15)–(A 16) and (A 30)–(A 31) within a periodic box $\hat{V}$. Where the micro-structural geometry of the acceptor/donor interface varies over the macroscopic lengthscale $\boldsymbol{x}$ (so that A_{ij}, B_{ij}, C_{ij} and b_{et} are all functions of $\boldsymbol{x}$), this requires that cell problems be solved at sufficient macroscopic spatial points in order to obtain a reasonable approximation to these functions in $\boldsymbol{x}$.

5 Comparison between full and homogenised models

The aims of this section are (i) to validate steady state solutions to the homogenised model (4.20)–(4.27) against steady-state solutions to the full model (2.22)–(2.31) in an interdigitated domain (see Figure 7) and (ii) to use the homogenised model to investigate device behaviour; in particular, we will calculate current–voltage curves for different device geometries (see Figure 8).

In Figure 7, we compare steady-state solutions of (4.20)–(4.27), the one-dimensional homogenised model (red curves), to those to (2.22)–(2.31), the full two-dimensional model (blue dashed curves). These simulations were performed for the set of parameters given in (3.2) in the geometry described in Section 3, namely with an interface $\partial\Omega_i$ given by $y = 0.7\cos(\delta\pi x)$. In terms of the homogenised model, this corresponds to setting $\alpha = -0.7$ and $\beta = 0.7$ and $F(y) = \frac{1}{\pi}\cos^{-1}(y/0.7)$. In order to compare the solutions to the one-dimensional homogenised model and the two-dimensional full model, we plot solutions of the full model (as functions of y) for p and ϕ along the line $x = 0$ and for n along the line $x = -\delta$ and compare to the equivalent solutions to the homogenised model (again plotted as a function of y). We obtain the steady-state solutions to the homogenised model (4.20)–(4.27) by numerically solving a steady-state form of the alternative formulation (4.28)–(4.33) using the Matlab boundary value problem solver 'bvp4c'.

Notably, the agreement between the two models is extremely good for $\Phi - \Phi_{bi} = -6$, it is still quite good for $\Phi = \Phi_{bi}$ but less good for $\Phi - \Phi_{bi} = 3$. As remarked in Section 3, it is a generic feature of the solutions to the full (two-dimensional) model, with applied potentials
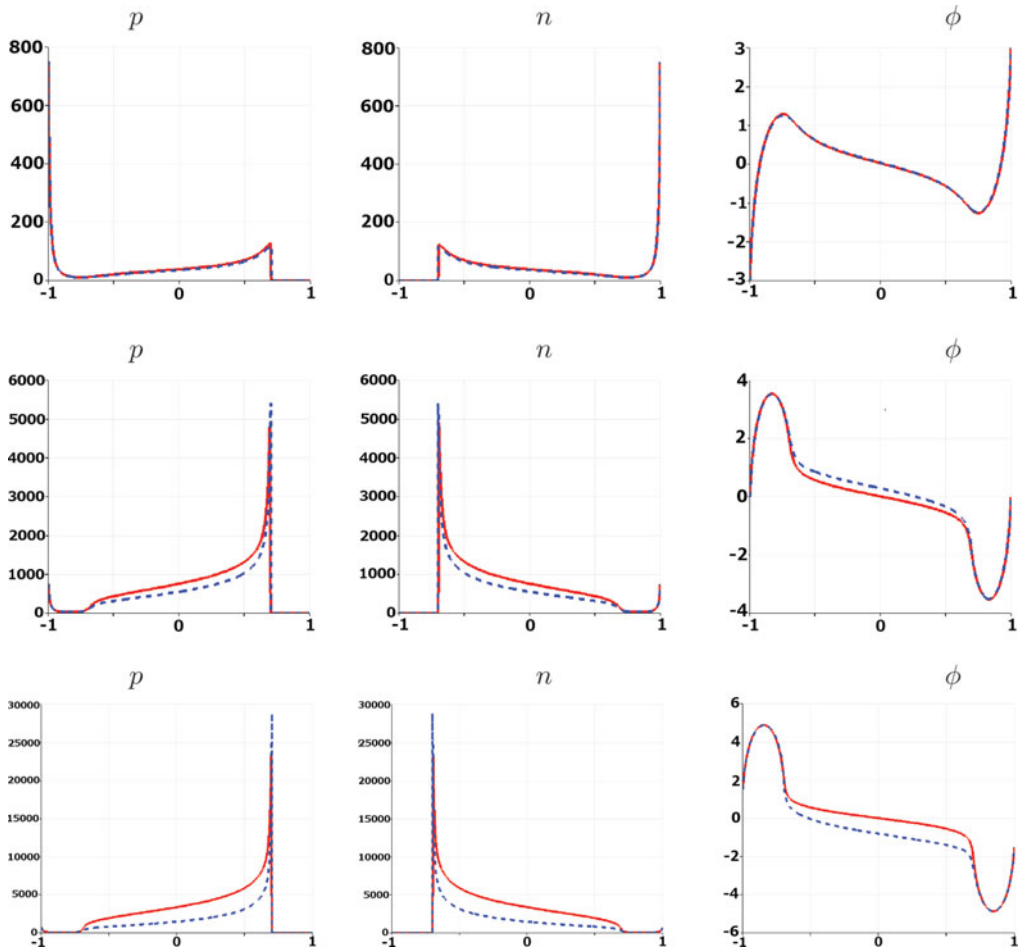
FIGURE 7. Comparison between solutions of the full dimensionless model (dashed blue line) and the homogenised model (solid red line), p_h, (left), n_h, (centre), ϕ_h, (right) for $\Phi - \Phi_{bi} = -6$ (upper), $\Phi - \Phi_{bi} = 0$ (middle), $\Phi - \Phi_{bi} = 3$ (lower). Here, plots of p_h and ϕ_h are made along the line $x = 0$, whereas those of n_h are made along $x = -\delta$. In all panels, the horizontal axis is the y-axis (stretching between -1 and 1).

$\Phi < \Phi_{bi}$, that it almost independent of the lateral dimension x and, as a corollary, it is well approximated by the solution to the homogenised model. The validity of the homogeneous approximation to the full model breaks down as the applied potential Φ increases above the built-in voltage as the solution develops features on the scale of the micro-structure. From a physical perspective, increases in applied potential act to counter the effect of the built-in voltage which is to drive electrons to the acceptor contact and holes to the donor contact. Thus, for large applied potentials electron and hole concentrations build up within the device leading to a shortening of the typical lengthscale for variations in the potential: The effective Debye length $L_{d,eff}$, which in this instance, can be estimated

from the relation:

$$L_{d,eff} = \left(\frac{(\epsilon_a \epsilon_d)^{1/2} kT}{q \rho_{eff}} \right)^{1/2},$$

where ρ_{eff} gives a measure of the charge density (caused by the electrons and holes). Once the effective Debye length decreases (with increases in Φ) to the lengthscale of the micro-structure, the solution starts exhibiting significant variations on the scale of the micro-structure, which invalidate the standard homogenisation procedure. Interestingly, in the instance of an interdigitated morphology, it is still possible to derive averaged equations by using a non-linear multiple scales method, but since the results have little bearing on the physically relevant power generating regime, we omit the details.

6 Device current–voltage curves calculated using the homogenised model

We finish by using the homogenised model to calculate current–voltage (J–V) curves for a range of device geometries. In order to make fair comparison between different devices, we plot J–V curves in which the current is rescaled with the maximum photocurrent γ_{eff}/K that can be extracted from the device assuming that all incident photons are absorbed to make excitons that reach the acceptor/donor interface (before recombination). Where the device has entire capping layers that prevent contact between the acceptor and the positive contact and between the donor and the negative contact, the solution of the homogenised model depends only on the built-in voltage Φ_{bi} and the applied potential Φ through $\Phi - \Phi_{bi}$, and so in these cases we plot KJ/γ_{eff} versus $\Phi - \Phi_{bi}$. In contrast where either (or both) the acceptor contacts the lower (hole extracting) electrode or the donor contacts the upper (electron extracting) electrode, the solution depends independently on Φ and Φ_{bi} and so we plot KJ/γ_{eff} versus Φ.

In Figure 8, we use the parameter set given in (3.2) with the exception that we take

$$\lambda = 0.1, \; \Gamma = 2 \times 10^{-6}, \; \beta_a = 0.5, \; \beta_d = 0.5, \; K = 2, \; \theta = 0, \tag{6.1}$$

noting, in particular, that the smaller values of β_a and β_d taken here, and consequently the less significant exciton recombination, give a significantly more efficient cell than the original parameter set. In the left-hand panel of Figure 8, we display J–V curves for four different bulk heterojunctions with capping layers of different thicknesses. The geometric properties of these heterojunctions are described by the following parameter sets:

- (I) $\alpha = -0.7$ and $\beta = 0.7$ and $F(y) = \frac{1}{\pi} \cos^{-1}(y/0.7)$ in $\alpha < y < \beta$,
- (II) $\alpha = -0.9$ and $\beta = 0.9$ and $F(y) = \frac{1}{\pi} \cos^{-1}(y/0.9)$ in $\alpha < y < \beta$,
- (III) $\alpha = -0.7$ and $\beta = 0.7$ and $F(y) = \frac{1}{2}$ in $\alpha < y < \beta$,
- (IV) $\alpha = -0.9$ and $\beta = 0.9$ and $F(y) = \frac{1}{2}$ in $\alpha < y < \beta$.

In all four of these geometries, the donor material does not directly contact the upper electrode $y = 1$ and the acceptor material does not directly contact the lower electrode $y = -1$. As can be seen the main feature of these curves is that their characteristics improve as the thickness $1 + \alpha$ of the lower donor blocking layer decreases (i.e., as α
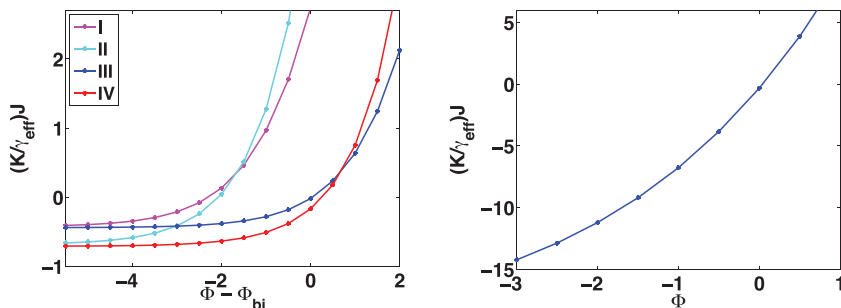
FIGURE 8. Current–voltage curves predicted by the homogenised model: left-hand panel for devices with capping layers and right-hand panel for a device without a capping layer. Parameter values and device geometry are described in Section 6.

decreases towards -1); the best reverse saturation current being for curves (II) and (IV) where the interface almost contacts the lower electrode. In particular, it can be seen that reverse saturation current (i.e., the current as $\Phi \to -\infty$) increases as the thickness of the blocking layer decreases. This is not particularly surprising because light enters from the surface $y = -1$ and its intensity decays rapidly as it propagates in the positive y-direction. Thus, much of the energy of the incident radiation is lost if the capping layer adjacent to the surface $y = -1$ is thick, and this is reflected in the relatively poor performance of the cell. Reducing this lower capping layer too far though is dangerous because it can result in direct contact between the acceptor region Ω_a and the positive contact (on $y = -1$) resulting in a short circuit. This phenomenon is illustrated in the right-hand panel of Figure 8 where we display the J–V curve for a device in which $F(y) \equiv 0.5$, so that the acceptor material contacts the lower (hole extracting) electrode and the donor material contacts the upper (electron extracting) electrode. The material parameters for this device are the same as those considered above (I)–(IV) but in addition we specify the built-in potential by $\Phi_{bi} = 10$. Here, it can be seen that the power generating capacity predicted by the model for this device is virtually non-existent since the open circuit voltage Φ_{oc} (i.e., the voltage Φ when $J = 0$) is close to zero, whereas in reality such devices are usually capable of producing power. The issue here is the use of Ohmic boundary conditions to describe the contacts made between acceptor with the lower electrode (hole extracting) and the donor with the upper (electron extracting) electrode. In well-designed devices, the energy of the donor HOMO (analogous to the valence band edge) lies close to the Fermi level of the hole extracting electrode and the energy of the acceptor LUMO (analogous to the conduction band edge) lies close to the Fermi level of the electron extracting electrode; this means that it is appropriate to use Ohmic conditions for such contacts. However, the same is not generally true for the energy differences between (a) the acceptor LUMO and the Fermi level of the hole extracting electrode and (b) the donor HOMO and the Fermi level of the electron extracting which means that Ohmic boundary conditions are inappropriate and need to be replaced by more general conditions describing charge recombination and injection processes taking place at the contact. The derivation of such boundary conditions describing the contact between an organic semiconductor and a metal has been made in [51]. However, this (as pointed out in [3]) leads to a final

statement of the boundary conditions that is inapplicable to solar cells because it neglects the diffusive fluxes of charge carriers; the correct conditions can be found in [3]. In the case where the equilibrium electron concentration n on the hole extracting contact and the equilibrium hole concentration p on the hole extracting contact are both very small (so that injection can be neglected), these boundary conditions take the (dimensional) form

$$\left.\frac{\partial n^*}{\partial x^*}\right|_{x^*=-L} \sim \left.\frac{n^*}{r_c\psi^2(E^*)}\right|_{x^*=L} \text{ and } \left.\frac{\partial p^*}{\partial x^*}\right|_{x^*=L} \sim -\left.\frac{p^*}{r_c\psi^2(E^*)}\right|_{x^*=L} \text{ for } E^* < 0, \quad (6.2)$$

where $\quad E^* = -\dfrac{\partial \phi^*}{\partial x^*}$ and $\psi(E^*) = \dfrac{1}{f} + \dfrac{1}{\sqrt{f}} - \dfrac{(1+2\sqrt{f})^{1/2}}{f}$ with $f = -q\dfrac{E^* r_c}{kT}$. $\quad (6.3)$

Here, r_c is the Coulomb radius defined by $r_c = q^2/(4\pi\varepsilon kT)$. Where the electric field has the opposite sign, these approximate boundary conditions should be replaced by

$$\left.\frac{\partial n^*}{\partial x^*}\right|_{x^*=-L} \sim \left.\frac{4n^*}{r_c}\right|_{x^*=L} \quad \text{and} \quad \left.\frac{\partial p^*}{\partial x^*}\right|_{x^*=L} \sim -\left.\frac{4p^*}{r_c}\right|_{x^*=L} \quad \text{for} \quad E^* > 0.$$

These boundary conditions are discussed in further detail in Section C.

7 Conclusions

In this work (in Section 2), we have formulated a model for charge transport and light absorption in an organic bulk heterojunction solar cell consisting of two organic semiconducting materials, one an electron donor and the other an electron acceptor, that contact each other along a highly convoluted interface. We used a finite element method, in Section 3, to solve the resulting coupled partial differential equations (at steady state) in a device with an interdigitated interface between the acceptor and donor materials (as illustrated in Figure 3) for a range of applied potentials. Motivated by these results we observed that the solution did not vary significantly over the scale of the micro-structure (i.e., it is almost independent of the lateral spatial variable x) when the applied potential is less than the built-in voltage. This led us, in Section 4, to use the method of multiple scales to derive a homogenised model, in which variables are averaged over the micro-structure. We did this both in the case of an interdigitated acceptor/donor interface and in the more generic case of a complex interlacing three-dimensional micro-structure, such as that commonly encountered in devices manufactured by spin-coating. In the former case, we compared the solutions from the systematically derived homogenised model to those of the full model (with realistic parameters) and found good agreement, provided the applied potential was less than the built in voltage. This is the device's power generating regime, and thus the most relevant one from the point of view of solar cell performance.

Although we did not perform simulations of the full model on an interlacing three-dimensional micro-structures, we note that such simulations have been performed in [35] (in realistic parameter regimes) and further, that to a good approximations, n and p vary solely in y, so that the electric field is predominantly in the y-direction, thus, supporting our effective medium approach. The result of the multiple scales analysis was a homogenised

model that, in dimensional form, can be written as

$$(1 - F(\boldsymbol{x}^*))q\frac{\partial p^*}{\partial t^*} + \nabla^* \cdot \langle \boldsymbol{j}_p^* \rangle + B_{et}^*(\boldsymbol{x}^*)(qR^*(n^*, p^*) - \langle j_{phot}^* \rangle) = 0, \tag{7.1}$$

$$F(\boldsymbol{x}^*)q\frac{\partial n^*}{\partial t^*} - \nabla^* \cdot \langle \boldsymbol{j}_n^* \rangle + B_{et}^*(\boldsymbol{x}^*)(qR^*(n^*, p^*) - \langle j_{phot}^* \rangle) = 0 \tag{7.2}$$

$$\langle \boldsymbol{j}_p^* \rangle = -\underline{\underline{\sigma}}_p^* \left(\nabla^* \phi^* + \frac{kT}{q}\nabla^* \log p^* \right), \qquad \langle \boldsymbol{j}_p^* \rangle = -\underline{\underline{\sigma}}_n^* \left(\nabla^* \phi^* - \frac{kT}{q}\nabla^* \log n^* \right), \tag{7.3}$$

$$\text{where} \quad \underline{\underline{\sigma}}_p^* = \frac{(D_nD_p)^{1/2}q^2}{kT}\underline{\underline{B}}p^*, \quad \text{and} \quad \underline{\underline{\sigma}}_n^* = \frac{(D_nD_p)^{1/2}q^2}{kT}\underline{\underline{C}}n^*, \tag{7.4}$$

$$\nabla^* \cdot \langle \mathcal{D}^* \rangle = q((1 - F(\boldsymbol{x}^*))p^* - F(\boldsymbol{x}^*)n^*), \quad \text{and} \quad \langle \mathcal{D}^* \rangle = -\underline{\underline{\epsilon}}^*\nabla^* \phi^*, \tag{7.5}$$

$$\text{where} \quad \underline{\underline{\epsilon}}^* = (\varepsilon_a\varepsilon_d)^{1/2}\underline{\underline{A}}. \tag{7.6}$$

Here, $B_{et}^*(\boldsymbol{x}^*)$ is the surface area of acceptor/donor interface per unit volume of material, and $\langle j_{phot}^* \rangle(\boldsymbol{x}^*)$ is the local average of the photocurrent over the surface area of the acceptor/donor interface; the averaged hole and electron currents $\langle \boldsymbol{j}_p^* \rangle$ and $\langle \boldsymbol{j}_n^* \rangle$ are given in terms of the electric potential by the generalised Ohm's Laws (7.3) in which the tensor hole and electron conductivities $\underline{\underline{\sigma}}_p^*$ and $\underline{\underline{\sigma}}_n^*$ are defined via (7.4) in terms of the dimensionless tensors $\underline{\underline{B}}$ and $\underline{\underline{C}}$ that characterise the micro-structure through the relations (4.39)–(4.40); the averaged electric displacement field $\langle \mathcal{D}^* \rangle$ is related to the electric potential by (7.5) in which the permittivity tensor $\underline{\underline{\epsilon}}^*$ is given by (7.6) in terms of the dimensionless tensor $\underline{\underline{A}}$, which characterises the micro-structure through the relation (4.41).

Finally, we used the homogenised model (as applied to an interdigitated cell) to investigate the effects that changes in the geometric properties of the cell have on its performance by calculating the current–voltage curves for a range of device designs, that make use of identical materials. We showed that for devices manufactured with capping layers it is important to ensure a relatively thin capping layer, above the lower transparent electrode, because the energy from light absorbed in the capping layer is lost to the device since excitons generated here are unlikely to reach the interface before recombination. However, reducing the thickness of this capping layer to zero so that the acceptor/donor interface contacts the lower electrode (such as in a device made by spin coating) results in short-circuit and consequent losses that manifest themselves in a reduction of the open-circuit voltage.

Acknowledgments

Appendix A Derivation of homogenised equations for a bulk heterojunction

In this appendix, we consider how to derive homogenised equations, over the device lengthscale, by explicitly taking account of the processes occurring on the heterojunction

microscale. This will be accomplished via the method of multiple scales (see, for example, [11]). In this instance, we operate on the dimensionless equations (2.22)–(2.31) in which the device lengthscale is of $O(1)$ and that of the micro-structure is $O(\delta)$, where $\delta \to 0$. Furthermore, we assume that the micro-structure is *locally* periodic inside a completely periodic array of boxes which we denote by $\hat{\Omega}_d \cup \hat{\Omega}_a$. Consider now one of these boxes $\hat{V}$, say, whose volume is split into a part $\hat{\Omega}_d$ occupied by the donor material and a part $\hat{\Omega}_a$ represents occupied by the acceptor (see Figure 6 for an example configuration). Furthermore we denote that part of the boundary to $\hat{\Omega}_a$ lying along the boundary of $\hat{V}$ by $\partial \hat{\omega}_a$ and that part lying along the interface between $\hat{\Omega}_a$ and $\hat{\Omega}_d$ by $\partial \hat{\Omega}$. Similarly we denote that part of the boundary to $\hat{\Omega}_d$ lying along the boundary of $\hat{V}$ by $\partial \hat{\omega}_d$ and that part lying along the interface between $\hat{\Omega}_a$ and $\hat{\Omega}_d$ by $\partial \hat{\Omega}$. For the sake of generality we allow the micro-structure to change slowly, over the $O(1)$ lengthscale, and it is in this sense that it is *locally* periodic.

A.1 A multiple scales formulation of the problem

We investigate the distinguished limit that κ, v, χ, β_d, β_a, G_a, $\mathcal{E}$, λ, Γ, and γ_{eff} are $O(1)$ while $\delta \to 0$. We then introduce a microscale variable $\hat{x}$ defined by

$$x = \delta \hat{x},$$

and look for a solution to our equations that is a function both of the microscale variable $\hat{x}$ and the device scale variable x. As is standard in such multiple scales calculations we look for a solution that is periodic in the microscale variable transform the gradient operator via $\nabla \to \nabla + \hat{\nabla}/\delta$. We can thus rewrite (2.22)–(2.31) in the form

$$\left. \begin{aligned} \delta \frac{\partial p}{\partial t} + \hat{\nabla} \cdot \boldsymbol{j}_p + \delta \nabla \cdot \boldsymbol{j}_p &= 0 \\ \boldsymbol{j}_p = -\frac{\kappa}{\delta} \left[\hat{\nabla} p + p \hat{\nabla} \phi + \delta (\nabla p + p \nabla \phi) \right] & \\ \delta^2 v \frac{\partial c_d}{\partial t} = \chi \left[\hat{\nabla}^2 c_d + 2 \nabla \cdot \hat{\nabla} c_d + \nabla^2 c_d \right] + Q(y) - \beta_d c_d & \end{aligned} \right\} \quad \text{in} \quad \hat{\Omega}_d, \qquad (A\,1)$$

$$\left. \begin{aligned} \delta \frac{\partial n}{\partial t} - \hat{\nabla} \cdot \boldsymbol{j}_n - \delta \nabla \cdot \boldsymbol{j}_n &= 0 \\ \boldsymbol{j}_n = \frac{1}{\delta \kappa} \left[\hat{\nabla} n - n \hat{\nabla} \phi + \delta (\nabla n - n \nabla \phi) \right] & \\ \delta^2 v \frac{\partial c_a}{\partial t} = \frac{1}{\chi} \left[\hat{\nabla}^2 c_a + 2 \nabla \cdot \hat{\nabla} c_a + \nabla^2 c_a \right] + G_a Q(y) - \beta_a c_a & \end{aligned} \right\} \quad \text{in} \quad \hat{\Omega}_a, \qquad (A\,2)$$

$$\hat{\nabla} \cdot \mathcal{D} + \delta \nabla \cdot \mathcal{D} = \frac{\delta}{\lambda^2} \left(\mathcal{H}_d p - (1 - \mathcal{H}_d) n \right) \qquad (A\,3)$$

$$\mathcal{D} = -\frac{1}{\delta} \left(\left(\mathcal{E} \mathcal{H}_d + \frac{1}{\mathcal{E}} (1 - \mathcal{H}_d) \right) (\hat{\nabla} \phi + \delta \nabla \phi) \right) \qquad (A\,4)$$

$$\boldsymbol{j}_n \cdot \boldsymbol{N}|_{\partial \hat{\Omega}} = \boldsymbol{j}_p \cdot \boldsymbol{N}|_{\partial \hat{\Omega}} = \delta (\Gamma R(n, p) - J_{phot}), \qquad c_d|_{\partial \Omega_i} = c_a|_{\partial \Omega_i} = 0, \qquad (A\,5)$$

where
$$J_{phot} = \delta\gamma_{eff}\left(\frac{1}{\chi}(\hat{\nabla}c_a + \nabla c_a)\Big|_{\partial\hat{\Omega}} - \chi(\hat{\nabla}c_d + \nabla c_d)\Big|_{\partial\hat{\Omega}}\right)\cdot N \qquad \text{on} \quad \partial\Omega_i, \quad \text{(A 6)}$$

and $n, \ p, \ \phi, \ \boldsymbol{j}_n, \ \boldsymbol{j}_p, \ c_d, \ c_a$ are periodic in $\hat{\boldsymbol{x}}$ over $\hat{V}$.   (A 7)

Here, $\mathcal{H}_d$ is the characteristic function for the donor region (i.e., $\mathcal{H}_d = 1$ in $\hat{\Omega}_d$ and zero in $\hat{\Omega}_a$) and $\mathcal{D}$ is the dimensionless electric displacement field.

A.1.1 *The Interface*

We make the standard assumption that variables are periodic in the shortscale variable $\hat{\boldsymbol{x}}$. This ensures that there are no secular growth terms in their asymptotic expansions (in powers of δ). In order to allow us to account for an acceptor/donor interface which not only varies on the microscale but can also show slow variations in its structure over the macroscale we follow [48] and [6] and define the interface $\partial\hat{\Omega}$ by the zero level set of the function $\psi(\boldsymbol{x}, \hat{\boldsymbol{x}})$ (that is by $\psi(\boldsymbol{x}, \hat{\boldsymbol{x}}) = 0$) choosing this function so that $\psi > 0$ in Ω_a and $\psi < 0$ in Ω_d. It follows that N the unit normal to the interface (directed from $\hat{\Omega}_d$ into $\hat{\Omega}_a$) is given by

$$N = \frac{\hat{\nabla}\psi + \delta\nabla\psi}{|\hat{\nabla}\psi + \delta\nabla\psi|}, \tag{A 8}$$

and that the interface conditions (A 5a) can be written in the form

$$\boldsymbol{j}_n \cdot (\hat{\nabla}\psi + \delta\nabla\psi)\big|_{\partial\hat{\Omega}} = \boldsymbol{j}_p \cdot (\hat{\nabla}\psi + \delta\nabla\psi)\big|_{\partial\hat{\Omega}} = \delta\left|\hat{\nabla}\psi + \delta\nabla\psi\right|(\Gamma R(n,p) - J_{phot}). \tag{A 9}$$

It is also useful to define the leading order approximation to the unit normal to the interface by

$$N_0 = \frac{\hat{\nabla}\psi}{|\hat{\nabla}\psi|}. \tag{A 10}$$

A.1.2 *Two useful results*

Following [48] we note the following results that prove useful in the derivation of the homogenised equations:

$$\nabla \cdot \int_{\hat{\Omega}_a} \boldsymbol{j}(\boldsymbol{x}, \hat{\boldsymbol{x}})\, d\hat{V} \sim \int_{\hat{\Omega}_a} \nabla \cdot \boldsymbol{j}\, d\hat{V} + \int_{\partial\hat{\Omega}} \frac{\boldsymbol{j} \cdot \nabla\psi}{|\hat{\nabla}\psi|}\, d\hat{S}, \tag{A 11}$$

$$\nabla \cdot \int_{\hat{\Omega}_d} \boldsymbol{j}(\boldsymbol{x}, \hat{\boldsymbol{x}})\, d\hat{V} \sim \int_{\hat{\Omega}_d} \nabla \cdot \boldsymbol{j}\, d\hat{V} - \int_{\partial\hat{\Omega}} \frac{\boldsymbol{j} \cdot \nabla\psi}{|\hat{\nabla}\psi|}\, d\hat{S}, \tag{A 12}$$

which are true for a differentiable vector field $\boldsymbol{j}(\boldsymbol{x}, \hat{\boldsymbol{x}})$ defined in $\hat{\Omega}_a$ and $\hat{\Omega}_d$, respectively.

A.2 Homogenisation of the potential equation

Substitution of the expansions (4.34) and

$$\mathcal{D} = \mathcal{D}_0(\boldsymbol{x}, \hat{\boldsymbol{x}}, t) + \delta \mathcal{D}_1(\boldsymbol{x}, \hat{\boldsymbol{x}}, t) + \delta^2 \mathcal{D}_2(\boldsymbol{x}, \hat{\boldsymbol{x}}, t) + \cdots$$

into (A 3)–(A 4) yields the following cell problem, in $\hat{V}$, for the first order correction to the potential, at leading order:

$$\hat{\nabla}^2 \phi_1 = 0 \quad \text{in} \quad \hat{\Omega}_a \quad \text{and} \quad \hat{\Omega}_d, \qquad \text{(A 13)}$$

$$\left(\hat{\nabla} \phi_1 |_{\partial \hat{\Omega}} - \mathcal{E}^2 \hat{\nabla} \phi_1 |_{\partial \hat{\Omega}} \right) \cdot \boldsymbol{N}_0 = -(1 - \mathcal{E}^2) \nabla \phi_0 \cdot \boldsymbol{N}_0, \qquad \phi_1 |_{\partial \hat{\Omega}} = \phi_1 |_{\partial \hat{\Omega}}. \qquad \text{(A 14)}$$

We can write the solution to this problem in terms of the three characteristic functions $\mu^{(i)}(\boldsymbol{x}, \hat{\boldsymbol{x}})$ (for $i = 1, 2, 3$), which satisfy the problems

$$\hat{\nabla}^2 \mu^{(i)} = 0 \quad \text{in} \quad \hat{\Omega}_a \quad \text{and} \quad \hat{\Omega}_d, \qquad \text{(A 15)}$$

$$\left(\hat{\nabla} \mu^{(i)} |_{\partial \hat{\Omega}} - \mathcal{E}^2 \hat{\nabla} \mu^{(i)} |_{\partial \hat{\Omega}} \right) \cdot \boldsymbol{N}_0 = -N_{0,i}, \qquad \mu^{(i)} |_{\partial \hat{\Omega}} = \mu^{(i)} |_{\partial \hat{\Omega}}, \qquad \text{(A 16)}$$

where $N_{0,i}$ is the i-th component of $\boldsymbol{N}_0$. The solution for ϕ has the form

$$\phi_1(\boldsymbol{x}, \hat{\boldsymbol{x}}) = -(1 - \mathcal{E}^2) \sum_{i=1}^{3} \frac{\partial \phi_0}{\partial x_i} \mu^{(i)}. \qquad \text{(A 17)}$$

Proceeding with the expansion of (A 3)–(A 4) to next order, we obtain the following problem:

$$\hat{\nabla} \cdot \mathcal{D}_1 + \nabla \cdot \mathcal{D}_0 = \frac{1}{\lambda^2} \left(\mathcal{H}_d p_0 - (1 - \mathcal{H}_d) n_0 \right) \qquad \text{in} \quad \hat{\Omega}_a \cup \hat{\Omega}_d,$$

$$\mathcal{D}_1 \quad \text{periodic in} \quad \hat{\boldsymbol{x}}.$$

Integrating this problem over $\hat{\Omega}_a \cup \hat{\Omega}_d$ and applying the divergence theorem yield

$$\int_{\partial(\hat{\Omega}_a \cup \hat{\Omega}_d)} \mathcal{D}_1 \cdot \boldsymbol{N} d\hat{S} + \int_{\hat{\Omega}_a \cup \hat{\Omega}_d} \nabla \cdot \mathcal{D}_0 d\hat{V} = \frac{1}{\lambda^2} (|\hat{\Omega}_d| p_0 - |\hat{\Omega}_a| n_0),$$

where $|\hat{\Omega}_d| = \int_{\hat{\Omega}_d} d\hat{V}$ and $|\hat{\Omega}_a| = \int_{\hat{\Omega}_a} d\hat{V}$. Since $\mathcal{D}_1$ is periodic in $\hat{\boldsymbol{x}}$, the first term in the above expression vanishes so that it can be rewritten as

$$\nabla \cdot \langle \mathcal{D}_0 \rangle = \frac{1}{\lambda^2} \left((1 - F(\boldsymbol{x})) p_0(\boldsymbol{x}, t) - F(\boldsymbol{x}) n_0(\boldsymbol{x}, t) \right), \qquad \text{(A 18)}$$

where $\langle \mathcal{D}_0 \rangle (\boldsymbol{x}, t)$ is the averaged value of $\mathcal{D}_0$ over the periodic cell $\hat{\Omega}_a \cup \hat{\Omega}_d$ and $F(\boldsymbol{x})$ is the volume fraction of the acceptor; these quantities can thus be expressed in the form

$$\langle \mathcal{D}_0 \rangle = \frac{\int_{\hat{\Omega}_a \cup \hat{\Omega}_d} \mathcal{D}_0 d\hat{V}}{|\hat{\Omega}_a| + |\hat{\Omega}_d|}, \qquad F(\boldsymbol{x}) = \frac{|\hat{\Omega}_a|}{|\hat{\Omega}_a| + |\hat{\Omega}_d|}. \qquad \text{(A 19)}$$

In order to complete the analysis it remains to evaluate $\langle \mathcal{D}_0 \rangle (x, t)$ in terms of the slowly varying variable $\phi_0(x, t)$. We note that, where we replace ϕ_1 by its solution (A 17) and use the Einstein summation convention, $\mathcal{D}_0$ has the form

$$\mathcal{D}_0 = -\left(\mathcal{E}\mathcal{H}_d + \frac{1}{\mathcal{E}}(1 - \mathcal{H}_d) \right) \left(\delta_{ij} - (1 - \mathcal{E}^2)\frac{\partial \mu^{(j)}}{\partial \hat{x}_i} \right) \frac{\partial \phi_0}{\partial x_j} e_i.$$

Here, e_i is the unit basis vector in the direction of the x_i-axis. Integrating $\mathcal{D}_0$ over $\hat{\Omega}_a \cup \hat{\Omega}_d$ and dividing by $|\hat{\Omega}_a| + |\hat{\Omega}_d|$ yield an expression for $\langle \mathcal{D}_0 \rangle (x, t)$ in terms of an effective permittivity tensor $\underline{A}$ (that is determined from the underlying microscale geometry) and the gradient of ϕ_0

$$\langle \mathcal{D}_0 \rangle = -A_{ij}\frac{\partial \phi_0}{\partial x_j} e_i, \qquad \text{where}$$

$$A_{ij} = \frac{1}{|\hat{\Omega}_a| + |\hat{\Omega}_d|} \int_{\hat{\Omega}_a \cup \hat{\Omega}_d} \left(\mathcal{E}\mathcal{H}_d + \frac{1}{\mathcal{E}}(1 - \mathcal{H}_d) \right) \left(\delta_{ij} - (1 - \mathcal{E}^2)\frac{\partial \mu^{(j)}}{\partial \hat{x}_i} \right) d\hat{V}. \tag{A 20}$$

The 'averaged' equations for the leading order potential are thus given by (A 18) and (A 20).

A.3 Homogenisation of the carrier equations

Here, we derive averaged carrier equations in an analogous way to that presented for the averaged potential equation. We begin by expanding (A 1) and (A 2) to leading order obtaining the following expressions for $j_{p,0}$ and $j_{n,0}$:

$$\hat{\nabla} \cdot j_{p,0} = 0 \quad \text{and} \quad j_{p,0} = -\kappa \left(\nabla p_0 + p_0 \nabla \phi_0 + \hat{\nabla} p_1 + p_0 \hat{\nabla} \phi_1 \right) \quad \text{in} \quad \hat{\Omega}_d, \tag{A 21}$$

$$\hat{\nabla} \cdot j_{n,0} = 0 \quad \text{and} \quad j_{n,0} = \frac{1}{\kappa} \left(\nabla n_0 - n_0 \nabla \phi_0 + \hat{\nabla} n_1 - n_0 \hat{\nabla} \phi_1 \right) \quad \text{in} \quad \hat{\Omega}_a. \tag{A 22}$$

The boundary conditions on this problem come from the leading order expansion of (A 9) and are

$$j_{p,0} \cdot N_0|_{\partial\hat{\Omega}} = j_{n,0} \cdot N_0|_{\partial\hat{\Omega}} = 0. \tag{A 23}$$

On noting that n_0, p_0, and ϕ_0 are independent of $\hat{x}$ and recalling that $\hat{\nabla}^2\phi_1 = 0$, we see that (A 21), (A 22) can be simplified to

$$\hat{\nabla}^2 p_1 = 0 \quad \text{in} \quad \hat{\Omega}_d, \tag{A 24}$$
$$\hat{\nabla}^2 n_1 = 0 \quad \text{in} \quad \hat{\Omega}_a. \tag{A 25}$$

Appropriate boundary conditions on these problems come from substitution of the expressions for $j_{p,0}$ and $j_{n,0}$, contained in (A 21)–(A 22), into (A 23) and the assumption that

solution is periodic in $\hat{\boldsymbol{x}}$; thus, the problems for p_1 and n_1 are closed by

$$\hat{\nabla} p_1 \cdot \boldsymbol{N}_0|_{\partial\hat{\Omega}} = -(\nabla p_0 + p_0 \nabla \phi_0) \cdot \boldsymbol{N}_0|_{\partial\hat{\Omega}} - p_0 \hat{\nabla} \phi_1 \cdot \boldsymbol{N}_0|_{\partial\hat{\Omega}}, \tag{A 26}$$

$$p_1 \quad \text{periodic in } \hat{\boldsymbol{x}}, \tag{A 27}$$

$$\hat{\nabla} n_1 \cdot \boldsymbol{N}_0|_{\partial\hat{\Omega}} = -(\nabla n_0 - n_0 \nabla \phi_0) \cdot \boldsymbol{N}_0|_{\partial\hat{\Omega}} + n_0 \hat{\nabla} \phi_1 \cdot \boldsymbol{N}_0|_{\partial\hat{\Omega}} \tag{A 28}$$

$$n_1 \quad \text{periodic in } \hat{\boldsymbol{x}}. \tag{A 29}$$

A.3.1 *The solution to the first-order problem in terms of characteristic functions*

The solutions to the two problems for p_1 and n_1 can be written in terms of the six characteristic functions $\zeta^{(i)}$ and $\eta^{(i)}$ (for $i = 1, 2, 3$) defined by the problems

$$\hat{\nabla}^2 \zeta^{(i)} = 0 \quad \text{in} \quad \hat{\Omega}_d, \qquad \hat{\nabla} \zeta^{(i)} \cdot \boldsymbol{N}_0 \Big|_{\partial\hat{\Omega}} = \boldsymbol{e}_i \cdot \boldsymbol{N}_0, \qquad \zeta^{(i)} \text{ periodic in } \hat{\boldsymbol{x}}, \tag{A 30}$$

$$\hat{\nabla}^2 \eta^{(i)} = 0 \quad \text{in} \quad \hat{\Omega}_a, \qquad \hat{\nabla} \eta^{(i)} \cdot \boldsymbol{N}_0 \Big|_{\partial\hat{\Omega}} = \boldsymbol{e}_i \cdot \boldsymbol{N}_0, \qquad \eta^{(i)} \text{ periodic in } \hat{\boldsymbol{x}}. \tag{A 31}$$

It follows from (A 24)–(A 29) and (A 30)–(A 31) that

$$p_1(\boldsymbol{x}, \hat{\boldsymbol{x}}, t) = -p_0(\boldsymbol{x}, t)\phi_1(\boldsymbol{x}, \hat{\boldsymbol{x}}, t) - \sum_{i=1}^{3} \boldsymbol{e}_i \cdot (\nabla p_0(\boldsymbol{x}, t) + p_0(\boldsymbol{x}, t)\nabla \phi_0(\boldsymbol{x}, t))\zeta^{(i)}(\boldsymbol{x}, \hat{\boldsymbol{x}}, t),$$

$$\tag{A 32}$$

$$n_1(\boldsymbol{x}, \hat{\boldsymbol{x}}, t) = n_0(\boldsymbol{x}, t)\phi_1(\boldsymbol{x}, \hat{\boldsymbol{x}}, t) - \sum_{i=1}^{3} \boldsymbol{e}_i \cdot (\nabla n_0(\boldsymbol{x}, t) - n_0(\boldsymbol{x}, t)\nabla \phi_0(\boldsymbol{x}, t))\eta^{(i)}(\boldsymbol{x}, \hat{\boldsymbol{x}}, t).$$

$$\tag{A 33}$$

A.3.2 *The first-order problems for the carrier fluxes*

Expanding (A 1a) and (A 2a) to first order yields

$$\frac{\partial p_0}{\partial t} + \nabla \cdot \boldsymbol{j}_{p,0} + \hat{\nabla} \cdot \boldsymbol{j}_{p,1} = 0 \qquad \text{in} \quad \hat{\Omega}_d, \tag{A 34}$$

$$\frac{\partial n_0}{\partial t} - \nabla \cdot \boldsymbol{j}_{n,0} - \hat{\nabla} \cdot \boldsymbol{j}_{n,1} = 0 \qquad \text{in} \quad \hat{\Omega}_a. \tag{A 35}$$

The corresponding interface conditions (obtained from the $O(\delta)$ expansions of (A 9)) are

$$\boldsymbol{j}_{p,1} \cdot \hat{\nabla}\psi \Big|_{\partial\hat{\Omega}} + \boldsymbol{j}_{p,0} \cdot \nabla\psi|_{\partial\hat{\Omega}} = |\hat{\nabla}\psi|(\Gamma R(n_0(\boldsymbol{x}, t), p_0(\boldsymbol{x}, t)) - J_{phot,0}(\boldsymbol{x}, \hat{\boldsymbol{x}}, t)), \tag{A 36}$$

for $\boldsymbol{j}_{p,1}$ periodic in $\hat{\boldsymbol{x}}$ and

$$\boldsymbol{j}_{n,1} \cdot \hat{\nabla}\psi \Big|_{\partial\hat{\Omega}} + \boldsymbol{j}_{n,0} \cdot \nabla\psi|_{\partial\hat{\Omega}} = |\hat{\nabla}\psi|(\Gamma R(n_0(\boldsymbol{x}, t), p_0(\boldsymbol{x}, t)) - J_{phot,0}(\boldsymbol{x}, \hat{\boldsymbol{x}}, t)), \tag{A 37}$$

for $\boldsymbol{j}_{n,1}$ periodic in $\hat{\boldsymbol{x}}$.

Integrating (A 34) over $\hat{\Omega}_d$, applying the divergence theorem and the conditions (A 36) gives

$$|\hat{\Omega}_d|\frac{\partial p_0}{\partial t} + \int_{\hat{\Omega}_d} \nabla \cdot \boldsymbol{j}_{p,0} d\hat{V} - \int_{\partial\hat{\Omega}} \boldsymbol{j}_{p,0} \cdot \frac{\nabla\psi}{|\hat{\nabla}\psi|} d\hat{S} + \int_{\partial\hat{\Omega}} d\hat{S}\left(\Gamma R(n_0, p_0) - \frac{\int_{\partial\hat{\Omega}} J_{phot,0} d\hat{S}}{\int_{\partial\hat{\Omega}} d\hat{S}}\right) = 0.$$

Applying the formula (A 11) to the above yields the following equation for $p_0(\boldsymbol{x}, t)$:

$$(1 - F(\boldsymbol{x}))\frac{\partial p_0}{\partial t} + \nabla \cdot \langle \boldsymbol{j}_{p,0}\rangle + b_{et}(\Gamma R(n_0(\boldsymbol{x}, t), p_0(\boldsymbol{x}, t)) - \langle J_{phot,0}\rangle(\boldsymbol{x}, t)) = 0, \qquad (A\,38)$$

where $F(\boldsymbol{x})$ is the volume fraction of acceptor (defined in (A 19)), while the averaged hole current $\langle \boldsymbol{j}_{p,0}\rangle$, the B.E.T surface area b_{et} (i.e., the surface area of interface per unit volume), and the average photocurrent $\langle J_{phot,0}\rangle$ are defined by

$$\langle \boldsymbol{j}_{p,0}\rangle = \frac{1}{|\hat{\Omega}_a| + |\hat{\Omega}_d|} \int_{\hat{\Omega}_d} \boldsymbol{j}_{p,0} d\hat{V}, b_{et} = \frac{1}{|\hat{\Omega}_a| + |\hat{\Omega}_d|} \int_{\partial\hat{\Omega}} d\hat{S}, \langle J_{phot,0}\rangle = \frac{\int_{\partial\hat{\Omega}} J_{phot,0} d\hat{S}}{\int_{\partial\hat{\Omega}} d\hat{S}},$$
$$(A\,39)$$

note that here $|\hat{V}| = |\hat{\Omega}_a| + |\hat{\Omega}_d|$ is the volume of the periodic box $\hat{V}$ and so b_{et} is a measure of the surface area of interface per unit volume of material.

We can obtain an evolution equation for n_0, analogous to (A 38), in a similar manner. We begin by integrating (A 35) over $\hat{\Omega}_a$, applying the divergence theorem and the boundary conditions (A 37) to obtain

$$|\hat{\Omega}_a|\frac{\partial n_0}{\partial t} - \int_{\hat{\Omega}_d} \nabla \cdot \boldsymbol{j}_{n,0} d\hat{V} - \int_{\partial\hat{\Omega}} \boldsymbol{j}_{n,0} \cdot \frac{\nabla\psi}{|\hat{\nabla}\psi|} d\hat{S} + \int_{\partial\hat{\Omega}} d\hat{S}(\Gamma R(n_0, p_0) - \langle J_{phot,0}\rangle) = 0.$$

Applying the formula (A 12) to yields the desired result

$$F(\boldsymbol{x})\frac{\partial n_0}{\partial t} - \nabla \cdot \langle \boldsymbol{j}_{n,0}\rangle + b_{et}(\Gamma R(n_0, p_0) - \langle J_{phot,0}\rangle) = 0, \qquad (A\,40)$$

where

$$\langle \boldsymbol{j}_{n,0}\rangle = \frac{1}{|\hat{\Omega}_a| + |\hat{\Omega}_d|} \int_{\hat{\Omega}_d} \boldsymbol{j}_{p,0} d\hat{V}. \qquad (A\,41)$$

It remains to determine the two quantities $\langle \boldsymbol{j}_{p,0}\rangle$ and $\langle \boldsymbol{j}_{n,0}\rangle$. This we do by substituting for p_1 and n_1, from (A 32) and (A 33), into the leading order expansions for $\boldsymbol{j}_{p,0}$ and $\boldsymbol{j}_{n,0}$, (A 21b) and (A 22b), to find

$$\boldsymbol{j}_{p,0} = -\kappa\left(\delta_{ij} - \frac{\partial\zeta^{(j)}}{\partial\hat{x}_i}\right)\left(\frac{\partial p_0}{\partial x_j} + p_0\frac{\partial\phi_0}{\partial x_j}\right)\boldsymbol{e}_i,$$

$$\boldsymbol{j}_{n,0} = \frac{1}{\kappa}\left(\delta_{ij} - \frac{\partial\eta^{(j)}}{\partial\hat{x}_i}\right)\left(\frac{\partial n_0}{\partial x_j} - n_0\frac{\partial\phi_0}{\partial x_j}\right)\boldsymbol{e}_i,$$

where δ_{ij} is the Kronecker delta function and we employ the Einstein summation convention. Substituting these expressions into the definitions of $\langle \boldsymbol{j}_{p,0}\rangle$ and $\langle \boldsymbol{j}_{n,0}\rangle$ contained in (A 39) and (A 41) yields the following expressions for the average fluxes in terms of

the 'conductivity' tensors $\underline{\underline{B}}$ and $\underline{C}$ (determined from the microscopic geometry) and the leading order solutions for n, p and ϕ:

$$\langle \boldsymbol{j}_{p,0} \rangle_i = -B_{ij} \left(\frac{\partial p_0}{\partial x_j} + p_0 \frac{\partial \phi_0}{\partial x_j} \right) \text{ where } B_{ij} = \frac{\kappa}{|\hat{\Omega}_d| + |\hat{\Omega}_a|} \int_{\hat{\Omega}_d} \left(\delta_{ij} - \frac{\partial \zeta^{(j)}}{\partial \hat{x}_i} \right) d\hat{V}, \quad \text{(A 42)}$$

$$\langle \boldsymbol{j}_{n,0} \rangle_i = C_{ij} \left(\frac{\partial n_0}{\partial x_j} - n_0 \frac{\partial \phi_0}{\partial x_j} \right) \text{ where } C_{ij} = \frac{1}{\kappa(|\hat{\Omega}_d| + |\hat{\Omega}_a|)} \int_{\hat{\Omega}_a} \left(\delta_{ij} - \frac{\partial \eta^{(j)}}{\partial \hat{x}_i} \right) d\hat{V}. \quad \text{(A 43)}$$

A.4 The exciton equation

The micro-structure is tuned to be roughly the same scale as the exciton decay length. It follows that exciton concentration depends, to leading order, upon not only the macroscale variable $\boldsymbol{x}$ but also on the microscale variable $\hat{\boldsymbol{x}}$. In terms of the multiple scale expansion, the exciton equations (2.22c) and (2.23c) and boundary condition (2.26b) become

$$\chi \left(\hat{\nabla}^2 c_d + 2\delta \nabla \cdot (\hat{\nabla} c_d) + \delta^2 \nabla^2 c_d \right) + Q(y) - \beta_d c_d = 0, \qquad \text{in} \quad \hat{\Omega}_d,$$

$$c_d|_{\partial\hat{\Omega}} = 0 \quad \text{and} \quad c_d \text{ periodic in } \hat{\boldsymbol{x}},$$

$$\frac{1}{\chi} \left(\hat{\nabla}^2 c_a + 2\delta \nabla \cdot (\hat{\nabla} c_a) + \delta^2 \nabla^2 c_a \right) + G_a Q(y) - \beta_a c_a = 0, \qquad \text{in} \quad \hat{\Omega}_a,$$

$$c_a|_{\partial\hat{\Omega}} = 0 \quad \text{and} \quad c_a \text{ periodic in } \hat{\boldsymbol{x}},$$

so that to leading order

$$\chi \hat{\nabla}^2 c_{d,0} + Q(y) - \beta_d c_{d,0} = 0, \qquad \text{in} \quad \hat{\Omega}_d,$$

$$c_{d,0}|_{\partial\hat{\Omega}} = 0 \quad \text{and} \quad c_{d,0} \text{ periodic in } \hat{\boldsymbol{x}},$$

$$\frac{1}{\chi} \hat{\nabla}^2 c_{a,0} + G_a Q(y) - \beta_a c_{a,0} = 0, \qquad \text{in} \quad \hat{\Omega}_a,$$

$$c_{a,0}|_{\partial\hat{\Omega}} = 0 \quad \text{and} \quad c_{a,0} \text{ periodic in } \hat{\boldsymbol{x}}.$$

The solution to these two problems can be used to determine $J_{phot,0}$ via

$$J_{phot,0}(\boldsymbol{x}, \hat{\boldsymbol{x}}, t) = \gamma_{eff} \left(\frac{1}{\chi} \hat{\nabla} c_{a,0}|_{\partial\hat{\Omega}} - \chi \hat{\nabla} c_{d,0}|_{\partial\hat{\Omega}} \right) \cdot \boldsymbol{N}_0,$$

and then $\langle J_{phot,0} \rangle(\boldsymbol{x}, t)$ is determined using (A 39c).

Appendix B Details of the numerical solution to the dimensionless model

B.1 Variational formulation of the dimensionless model

In order to derive a finite element approximation of the non-dimensional model (2.22)–(2.31), we first write it in variational form. To this end we introduce

$$\mathcal{W}_d := \{\eta(x, y, t) \in L^2(0, T; H^1(\Omega_d)) | \ \eta(x, -1, t) = 0\},$$

$$\widehat{\mathcal{W}}_d := \{\eta(x, y, t) \in L^2(0, T; H^1(\Omega_d)) | \ \eta|_{\partial\Omega_i} = 0\},$$

$$\mathcal{W}_a := \{\eta(x,y,t) \in L^2(0,T;H^1(\Omega_a)) |\ \eta(x,1,t) = 0\},$$

$$\widehat{\mathcal{W}}_a := \{\eta(x,y,t) \in L^2(0,T;H^1(\Omega_a)) |\ \eta|_{\partial\Omega_i} = 0\},$$

and for simplicity of notation we drop the $*$ superscript.

From the first and second equations in (2.22), we obtain

$$\frac{\partial p}{\partial t} = \nabla \cdot [\kappa(\nabla p + p\nabla\phi)] \quad \text{in } \Omega_d,$$

and multiplying this equation by $\eta \in \mathcal{W}_d$ and integrating over Ω_d, we have

$$\int_{\Omega_d} \left(\frac{\partial p}{\partial t}\eta + \kappa(\nabla p + p\nabla\phi) \cdot \nabla\eta \right) = \kappa \int_{\partial\Omega_i} (\nabla p + p\nabla\phi) \cdot \boldsymbol{N}\eta \quad \forall \eta \in \mathcal{W}_d,$$

and similarly from the first and second equations in (2.23), we obtain

$$\int_{\Omega_a} \left(\frac{\partial n}{\partial t}\xi + \frac{1}{\kappa}(\nabla n - n\nabla\phi) \cdot \nabla\xi \right) = -\frac{1}{\kappa} \int_{\partial\Omega_i} (\nabla n - n\nabla\phi) \cdot \boldsymbol{N}\xi \quad \forall \xi \in \mathcal{W}_a.$$

From (2.26), we have

$$\int_{\Omega_d} \left(\frac{\partial p}{\partial t}\eta + \kappa(\nabla p + p\nabla\phi) \cdot \nabla\eta \right) = \delta\kappa \int_{\partial\Omega_i} (J_{phot}(c_a,c_d) - \Gamma R(n,p))\eta \quad \forall \eta \in \mathcal{W}_d, \quad \text{(B 1)}$$

$$\int_{\Omega_a} \left(\frac{\partial n}{\partial t}\xi + \frac{1}{\kappa}(\nabla n - n\nabla\phi) \cdot \nabla\xi \right) = \frac{\delta}{\kappa} \int_{\partial\Omega_i} (J_{phot}(c_a,c_d) - \Gamma R(n,p))\xi \quad \forall \xi \in \mathcal{W}_a, \quad \text{(B 2)}$$

where from (2.31) we have

$$J_{phot}(c_a,c_d) = \delta\gamma_{eff} \left(\frac{1}{\chi}\nabla c_a \bigg|_{\partial\Omega_i} - \chi\nabla c_d \bigg|_{\partial\Omega_i} \right) \cdot \boldsymbol{N}. \quad \text{(B 3)}$$

Multiplying (2.24) by $\eta \in \mathcal{W}_d$ and integrating over Ω_d, we obtain

$$\int_{\Omega_d} \mathcal{E}\nabla\phi \cdot \nabla\eta = \frac{1}{\lambda^2} \int_{\Omega_d} p\eta + \int_{\partial\Omega_i} \eta\mathcal{E}\nabla\phi \cdot \boldsymbol{N} \quad \forall \eta \in \mathcal{W}_d,$$

and similarly multiplying (2.24) by $\xi \in \mathcal{W}_a$ and integrating over Ω_a, we obtain

$$\int_{\Omega_a} \frac{1}{\mathcal{E}}\nabla\phi \cdot \nabla\xi = -\frac{1}{\lambda^2} \int_{\Omega_a} n\xi - \int_{\partial\Omega_i} \frac{\xi}{\mathcal{E}}\nabla\phi \cdot \boldsymbol{N} \quad \forall \xi \in \mathcal{W}_a.$$

Combining the two equations above gives the following for all $\eta \in \mathcal{W}_d$ and for all $\xi \in \mathcal{W}_a$:

$$\int_{\Omega_a} \nabla\phi \cdot \nabla\xi + \int_{\Omega_d} \nabla\phi \cdot \nabla\eta = \frac{1}{\mathcal{E}\lambda^2} \int_{\Omega_d} p\eta - \frac{\mathcal{E}}{\lambda^2} \int_{\Omega_a} n\xi + \int_{\partial\Omega_i} \left(\eta\mathcal{E} - \frac{\xi}{\mathcal{E}} \right) \nabla\phi \cdot \boldsymbol{N}. \quad \text{(B 4)}$$

Multiplying the third equation in (2.22) by $\eta \in \widehat{\mathcal{W}}_d$ and integrating over Ω_d, we have

$$\int_{\Omega_d} \left(\delta^2 v \frac{\partial c_d}{\partial t} + \beta_d c_d \right) \eta + \delta^2\chi \int_{\Omega_d} \nabla c_d \cdot \nabla\eta = \int_{\Omega_d} Q(y)\eta \quad \forall \eta \in \widehat{\mathcal{W}}_d, \quad \text{(B 5)}$$

and similarly multiplying the third equation in (2.22) by $\xi \in \widehat{\mathcal{W}}_a$ and integrating over Ω_a, we have

$$\int_{\Omega_a} \left(\delta^2 v \frac{\partial c_a}{\partial t} + \beta_a c_a \right) \xi + \frac{\delta^2}{\chi} \int_{\Omega_a} \nabla c_a \cdot \nabla \xi = \int_{\Omega_a} G_a Q(y) \xi \quad \forall \xi \in \widehat{\mathcal{W}}_a. \tag{B 6}$$

B.2 Finite element approximation

Let Ω be a rectangular domain. Let $\mathcal{T}^h$ be a partitioning of Ω into J disjoint open simplices σ, with $h_\sigma := \mathrm{diam}(\sigma)$ and $h := \min_{\sigma \in \mathcal{T}^h} h_\sigma$, so that $\overline{\Omega} = \cup_{\sigma \in \mathcal{T}^h} \overline{\sigma}$. Furthermore, let $\mathcal{T}^h$ be such that the approximate curve $\partial \Omega_i^h$ comprises of triangle edges and each triangle, σ_j, $j = 1 \to J$, lies entirely in Ω_d^h or Ω_a^h. Associated with $\mathcal{T}^h$ are the finite element spaces

$$S^h = \{ \chi \in H^1(\Omega) | \ \chi|_{\sigma_j} \text{ is piecewise linear for } j = 1 \to J \},$$

$$S_d^h = \{ \chi \in H^1(\Omega_d^h) | \ \chi|_{\sigma_j} \text{ is piecewise linear for } j = 1 \to J \text{ and } \chi(x, -1) = 0 \},$$

$$S_a^h = \{ \chi \in H^1(\Omega_a^h) | \ \chi|_{\sigma_j} \text{ is piecewise linear for } j = 1 \to J \text{ and } \chi(x, 1) = 0 \},$$

$$\hat{S}_d^h = \{ \chi \in H^1(\Omega_d^h) | \ \chi|_{\sigma_j} \text{ is piecewise linear for } j = 1 \to J \text{ and } \chi|_{\partial \Omega_i^h} = 0 \},$$

$$\hat{S}_a^h = \{ \chi \in H^1(\Omega_a^h) | \ \chi|_{\sigma_j} \text{ is piecewise linear for } j = 1 \to J \text{ and } \chi|_{\partial \Omega_i^h} = 0 \},$$

$$S_\phi^h = \{ \chi \in S^h | \ \chi(x, -1) = (\Phi - \Phi_{bi})/2 \text{ and } \chi(x, 1) = -(\Phi - \Phi_{bi})/2 \},$$

$$S_p^h = \{ \chi \in S_d^h | \ \chi(x, -1) = \frac{\hat{n}}{\Upsilon} \}, \quad S_n^h = \{ \chi \in S_a^h | \chi(x, 1) = \hat{n} \Upsilon \},$$

$$S_c^h = \{ \chi \in S^h | \ \chi|_{\partial \Omega_i^h} = 0 \}.$$

In addition to $\mathcal{T}^h$, let $0 = t_0 < t_1 < \cdots < t_{N-1} < t_N = T$ be a partitioning of $[0, T]$ into possibly variable time steps $\tau_k := t_k - t_{k-1}$, $k = 1 \to N$.

The model (B 4)–(B 6) comprises of a system of strongly coupled partial differential equations, however by using a semi-implicit backward Euler finite element approximation it can be reduced to an uncoupled system of linear equations, see below, for the approximate solutions c_h^k, ϕ_h^k, p_h^k and n_h^k. In order to obtain the solution at the k-th time step, from the data for p_h^{k-1}, n_h^{k-1} and c^{k-1} at the $k-1$-th time step, we first solve (B 7) and (B 8) for c_h^k, before solving (B 9) for ϕ_h^k and finally use these results (together with the data from the $k-1$-th time step) to solve (B 10) and (B 11) for p_h^k and n_h^k. To ensure positivity of p_h^k and n_h^k at the k-th time step, we choose τ_k so that it satisfies the standard CFL condition that relates h to $|\nabla \phi_h^k|$.

This gives rise to the following finite element approximation of (B 4)–(B 6).

Given $\{p_h^{k-1}, n_h^{k-1}, c_{d,h}^{k-1}, c_{a,h}^{k-1}\} \in S_p^h \times S_n^h \times S_c^h$ find $\{p_h^k, n_h^k, \phi_h^k, c_{d,h}^k, c_{a,h}^k\} \in S_p^h \times S_n^h \times S_\phi^h \times S_c^h$ such that

$$\int_{\Omega_d} \left(\delta^2 v \frac{(c_{d,h}^k - c_{d,h}^{k-1})}{\tau_k} + \beta_d c_{d,h}^k \right) \eta + \delta^2 \chi \int_{\Omega_d} \nabla c_{d,h}^k \cdot \nabla \eta = \int_{\Omega_d} Q(y) \eta \quad \forall \eta \in \hat{S}_d^h, \tag{B 7}$$

$$\int_{\Omega_a} \left(\delta^2 v \frac{(c_{a,h}^k - c_{a,h}^{k-1})}{\tau_k} + \beta_a c_{a,h}^k \right) \xi + \frac{\delta^2}{\chi} \int_{\Omega_a} \nabla c_{a,h}^k \cdot \nabla \xi = \int_{\Omega_a} G_a Q(y) \xi \quad \forall \xi \in \hat{S}_a^h, \quad \text{(B 8)}$$

$$\int_{\Omega_a} \nabla \phi_h^k \cdot \nabla \xi + \int_{\Omega_d} \nabla \phi_h^k \cdot \nabla \eta - \int_{\partial \Omega_i} \left(\eta \mathcal{E} - \frac{\xi}{\mathcal{E}} \right) \nabla \phi_h^k \cdot \mathbf{N}$$
$$= \frac{1}{\mathcal{E} \lambda^2} \int_{\Omega_d} p_h^{k-1} \eta - \frac{\mathcal{E}}{\lambda^2} \int_{\Omega_a} n_h^{k-1} \xi \forall (\eta, \xi) \in S_d^h \times S_a^h, \quad \text{(B 9)}$$

$$\int_{\Omega_d} \left(\frac{(p_h^k - p_h^{k-1})}{\tau_k} \eta + \kappa (\nabla p_h^k + p_h^k \nabla \phi_h^k) \cdot \nabla \eta \right)$$
$$= \delta \kappa \int_{\partial \Omega_i^h} \left(J_{phot}(c_{a,h}^k, c_{d,h}^k) - \Gamma R(n_h^{k-1}, p_h^{k-1}) \right) \eta \quad \forall \eta \in S_d^h, \quad \text{(B 10)}$$

$$\int_{\Omega_a} \left(\frac{(n_h^k - n_h^{k-1})}{\tau_k} \xi + \frac{1}{\kappa} (\nabla n_h^k - n_h^k \nabla \phi_h^k) \cdot \nabla \xi \right)$$
$$= \frac{\delta}{\kappa} \int_{\partial \Omega_i^h} \left(J_{phot}(c_{a,h}^k, c_{d,h}^k) - \Gamma R(n_h^{k-1}, p_h^{k-1}) \right) \xi \quad \forall \xi \in S_a^h. \quad \text{(B 11)}$$

Here,

$$J_{phot}(c_{a,h}^k, c_{d,h}^k) = \delta \gamma_{eff} \left(\frac{1}{\chi} \nabla c_{a,h}^k \bigg|_{\partial \Omega_i} - \chi \nabla c_{d,h}^k \bigg|_{\partial \Omega_i} \right) \cdot \mathbf{N}.$$

Remark: The non-dimensionalised model (B 4)–(B 6) and the corresponding finite element approximation are formulated for a geometry in two space directions; however, both the model and the finite element approximation can be naturally extended to three space dimensions.

Appendix C The charge injection/extraction boundary conditions

According to [3, 51] the boundary conditions at metal contact depend upon the electric field at that contact. In particular, if the field acts to drive a particular type of charge carrier from the metal contact into the organic semiconductor, there is a competition between the electric field (that drives the carrier away from the metal contact) and the image charge (that attracts it toward the contact). There is thus a potential barrier to charge injection and a distance r_c (the Coulomb) radius within which a charge carrier is very likely to recombine with the metal interface (because of the effect of its image). The Coulomb radius is given by $r_c = q^2/(4\pi \varepsilon k T)$.

Here, we are primarily interested in the shorting contacts made between the acceptor- and the hole-extracting electrode (on $x = -L$) and the donor- and electron-extracting electrode (on $x = L$). In both these cases, a negative electric field ($E^* < 0$) drives charge carriers into the semiconductor from the contacts and according to [3, 51] the resulting

electron current (on $x = -L$) and hole current (on $x = L$) are given by

$$j_n^*|_{x^*=-L} = \frac{4\pi\varepsilon\mu_n(kT)^2}{q^2}\left(\frac{n^*}{\psi^2(E^*)} - 4N_0\exp\left(-\frac{U_{B1}}{kT} + f^{1/2}\right)\right) + q\mu_n E^* n^*\Big|_{x^*=-L}, \quad \text{(C 1)}$$

$$j_p^*|_{x^*=L} = \frac{4\pi\varepsilon\mu_p(kT)^2}{q^2}\left(\frac{p^*}{\psi^2(E^*)} - 4N_0\exp\left(-\frac{U_{B2}}{kT} + f^{1/2}\right)\right) + q\mu_p E^* p^*\Big|_{x^*=L}, \quad \text{(C 2)}$$

for $E^*|_{x^*=-L} < 0$ and $E^*|_{x^*=L} < 0$, respectively. Here, $\mu_n = qD_n/kT$ and $\mu_p = qD_p/kT$ are electron and hole mobilities, respectively, N_0 the density of chargeable sites in the semiconductor, U_{B1} and U_{B2} the Schottky barrier energies for electron injection on $x = -L$ and hole injection on $x = L$, respectively, and the dimensionless electric field f and the function $\psi(E^*)$ are defined in (6.3). If we now equate the left-hand sides of (C 1) and (C 2) with (2.3) and (2.4), we obtain the following conditions:

$$\frac{n^*}{4\psi^2(E^*)} - \frac{r_c}{4}\frac{\partial n^*}{\partial x^*}\Big|_{x^*=-L} = N_0\exp\left(-\frac{U_{B1}}{kT} + f^{1/2}\right) \quad \text{for} \quad E^*|_{x^*=-L} < 0, \quad \text{(C 3)}$$

$$\frac{p^*}{4\psi^2(E^*)} + \frac{r_c}{4}\frac{\partial p^*}{\partial x^*}\Big|_{x^*=L} = N_0\exp\left(-\frac{U_{B2}}{kT} + f^{1/2}\right) \quad \text{for} \quad E^*|_{x^*=L} < 0. \quad \text{(C 4)}$$

There are two interesting limits to these boundary conditions. The first is for small gradients in carriers concentration and for E^* sufficiently small such that $f \ll 1$ and $\psi \sim 1/2$; this gives the Ohmic boundary conditions $n^*|_{x^*=-L} \sim N_0\exp(-\frac{U_{B1}}{kT})$ and $p^*|_{x^*=L} \sim N_0\exp(-\frac{U_{B2}}{kT})$. The second, which is the relevant limit for these shorting contacts, is the limit of large Schottky barrier heights $U_{B1}/kT \gg 1$ and $U_{B2}/kT \gg 1$. This implies that the terms on right-hand side of (C 3)–(C 4) are negligible, giving the limit conditions (6.2).

In the case of positive electric fields $E^* > 0$, so that there are no injection barriers, the relevant boundary conditions, given in [3], are

$$j_n^*|_{x^*=-L} = \frac{16\pi\varepsilon\mu_n(kT)^2}{q^2}\left(n^* - N_0\exp\left(-\frac{U_{B1} + qE^* r_c/4}{kT}\right)\right)\Big|_{x^*=-L}, \quad \text{(C 5)}$$

$$j_p^*|_{x^*=L} = \frac{16\pi\varepsilon\mu_p(kT)^2}{q^2}\left(p^* - N_0\exp\left(-\frac{U_{B2} + qE^* r_c/4}{kT}\right)\right)\Big|_{x^*=L}. \quad \text{(C 6)}$$

Equating these equations with (2.3) and (2.4), as before, we obtain

$$n^*\left(1 - \frac{qr_c}{4kT}E^*\right) - \frac{r_c}{4}\frac{\partial n^*}{\partial x^*}\Big|_{x^*=-L} = N_0\exp\left(-\frac{U_{B1} + qE^* r_c/4}{kT}\right) \quad \text{for} \quad E^*|_{x^*=-L} > 0,$$
$$\text{(C 7)}$$

$$p^*\left(1 - \frac{qr_c}{4kT}E^*\right) + \frac{r_c}{4}\frac{\partial p^*}{\partial x^*}\Big|_{x^*=L} = N_0\exp\left(-\frac{U_{B2} + qE^* r_c/4}{kT}\right) \quad \text{for} \quad E^*|_{x^*=L} > 0,$$
$$\text{(C 8)}$$

and the appropriate limit equations for large barrier heights are (6.4).

References

[1] ALLAIRE, G. (1992) Homogenization and two-scale convergence. *SIAM J. Math. Anal.* **23**, 1482–1518.

[2] ALLSOP, N., NÜRNBERG, R., LUX-STEINER, M. CH. & SCHEDEL-NIEDRIG, TH. (2009) Three-dimensional simulations of a thin film heterojunction solar cell with a point contact/defect passivation structure at the heterointerface. *Appl. Phys. Lett.* **95**, 122108-1–122108-3.

[3] BARKER, J. A., RAMSDALE, C. M. & GREENHAM, N. C. (2003) Modelling the current-voltage characteristic of bilayer polymer devices. *Phys. Rev. B* **67**, 075205.

[4] BARRETT, J. W. & ELLIOTT, C. M. (1987) Fitted and unfitted finite-element methods for elliptic equations with smooth interfaces. *IMA J. Numer. Anal.* **7** 283–300.

[5] BRAUN, C. L. (1984) Electric-field assisted dissociation of charge-transfer states as a mechanism for photocarrier production. *Chem. Phys.* **80**, 4157–4161.

[6] BRUNA, M. & CHAPMAN, S. J. (2015) Diffusion in spatially varying porous media. *SIAM J.Appl. Maths.* **75**, 1648–1674.

[7] BRINKMAN, D., FELLNER, K., MARKOWICH, P. A. & WOLFRAM, M.-T. (2013) A drift-diffusion-reaction model for excitonic photovoltaic bilayers: Asymptotic analysis and a 2-D HDG finite-element scheme. *Math. Models Methods Appl. Sci.* **23**, 839–872.

[8] BUXTON, G. A. & CLARKE, N. (2006) Predicting structure and property relations in polymeric photovoltaic devices. *Phys. Rev. B* **74**, 085207.

[9] BUXTON, G. A. & CLARKE, N. (2007) Computer simulation of polymer solar cells. *Model. Simul. Mater. Sci. Eng.* **15**, 13–26.

[10] CHEN, J.-D., CUI, C., LI, Y.-Q., ZHOU, L., OU, Q.-D., LI, C., LI, Y. & TANG, J.-X. (2015) Single-junction polymer solar cells exceeding 10% power conversion efficiency. *Adv. Mater.* **27**, 1035–1041.

[11] COLE, J. D. (1995) Limit process expansions and homogenization. *SIAM J. Appl. Math.* **55**, 410–424.

[12] CLARKE, T. M. & DURRANT, J. R. (2010) Charge photogeneration in organic solar cells. *Chem. Rev.* **110**, 6736–6767.

[13] CLOVER, I. (2016) Heliatek raises bar for OPV efficiency to 13.2. *pv magazine.*

[14] CIORANESCU, D. & DONATO, P. (1999) *An Introduction to Homogenization,* Oxford Lecture Series in Mathematics and its Applications, Oxford, Oxford University Press.

[15] CREDGINGTON, D., KIM, Y., LABRAM, J., ANTHOPOULOS, T. D. & DURRANT, J. (2011) Analysis of recombination in polymer C60 solar cells. *J. Phys. Chem. Lett.* **2**, 2759.

[16] CREDGINGTON, D., JAMIESON, F. C., WALKER, B., NGUYEN, T.-Q. & DURRANT, J. R. (2012) Quantification of geminate and non-geminate recombination losses within a solution-processed small-molecule bulk heterojunction solar cell. *Adv. Mater.* **24**, 2135–2141.

[17] CRONE, B. K., DAVIDS, P. S., CAMPBELL, I. H. & SMITH, D. L. (2000) Device model investigation of bilayer organic light emitting diodes. *J. Appl. Phys.* **87**, 1974.

[18] DAVIDS, P. S., CAMPBELL, I. H. & SMITH, D. L. (1997) Device model for single carrier organic diodes. *J. Appl. Phys.* **82**, 6319.

[19] DE FALCO, C., SACCO, R. & VERRI, M. (2010) Analytical and numerical study of photocurrent transients in organic polymer solar cells. *Comput. Methods Appl. Mech. Eng.* **199**, 1722–1732.

[20] DEIBEL, C. & DYAKONOV, V. (2010) Polymer-fullerene bulk heterojunction solar cells. *Rep. Prog. Phys.* **73**, 096401.

[21] FOSTER, J. M., KIRKPATRICK, J. & RICHARDSON, G. (2013) Asymptotic and numerical prediction of current-voltagecurves for an organic bilayer solar cell under varying illumination and comparison to the Shockley equivalent circuit. *J. Appl. Phys.* **114**, 104501.

[22] GAJEWSKI, H., KAISER, H. CHR., LANGMACH, H., NÜRNBERG, R. & RICHTER, R. H. (2003) Mathematical modelling and numerical simulation of semiconductor detectors. In: W. Jäger & H. J. Krebs (editors), *Mathematics? Key Technology for the Future,* Springer, Berlin, Heidelberg, pp. 355–364.

[23] GAJEWSKI, H. *et al.* TeSCA *Two- and Three-Dimensional Semi-Conductor Analysis Package*, Weierstrass Institute for Applied Analysis and Stochastics, Berlin.

[24] GÜNES, S., NEUGEBAUER, H. & SARICIFTCI, N. S. (2007) Conjugated polymer-based organic solar cells. *Chem. Rev.* **103**, 1324.

[25] GREGG, K. A. & HANNA, M. C. (2003) Comparing organic to inorganic photovoltaic cells: Theory, experiment, and simulation. *J. Appl. Phys.* **93**, 3605–3614.

[26] GROVES, C., BLAKESLEY, J. C. & GREENHAM, N. C. (2010) Effect of charge trapping on geminate recombination and polymer solar cell performance. *Nano Lett.* **10**, 1063–1069.

[27] GROVES, C., KIMBER, R. G. E. & WALKER, A. B. (2010) Simulation of loss mechanisms in organic solar cells. *J. Chem. Phys.* **133**, 144110.

[28] HOPPE, H. & SARICIFTCI, N. S. (2004) Organic solar cells: An overview. *J. Mater. Res.* **19**, 1924–1945.

[29] DE JONGH, P. E. & VANMAEKELBERGH, D. (1996) Trap-limited transport in assemblies of nanometer-size TiO_2 particles. *Phys. Rev. Lett.* **77**, 3427–3430.

[30] KELLER, J. B. (1980) Darcy's law for flow in porous media and the two-space method. In: *Lecture Notes in Pure and Applied Mathematics* vol. 54, Dekker, New York.

[31] KELLER, J. B. (1977) Effective behavior of heterogeneous media. In: U. Landman (editor), *Statistical Mechanics and Statistical Methods in Theory and Application*, Plenum, New York, pp. 631–644.

[32] KIMBER, R. G. E., WRIGHT, E. N., O'KANE, S. E. J., WALKER, A. B. & BLAKESLEY, J. C. (2012) Mesoscopic kinetic Monte Carlo modeling of organic photovoltaic device characteristics. *Phys. Rev. B* **86**, 235206.

[33] KIRCHARTZ, T., PIETERS, B. E., KIRKPATRICK, J., RAU, U. & NELSON, J. (2011) Recombination via tail states in polythiophene: Fullerene solar cells. *Phys. Rev. B* **83**, 115209.

[34] KIRKPATRICK, J., MARCON, V., KREMER, K., NELSON, J. & ANDRIENKO, D. (2007) Charge mobility in discotic mesophases: A multiscale quantum and classical study. *Phys. Rev. Lett.* **98**, 227402.

[35] KODALI, H. K. & GANAPATHYSUBRAMANIAN, B. (2012) Computer simulation of heterogeneous polymer photovoltaic devices. *Model. Simul. Mater. Sci. Eng.* **20**, 035015.

[36] KOSTER, L. J. A., SMITS, E. C. P., MIHAILETCHI, V. D. & BLOM, P. W. M. (2005) Device model for the operation of polymer/fullerene bulk heterojunction solar cells. *Phys. Rev. B.* **72**, 085205.

[37] KOTLARSKI, J. D., BLOM, P. W., KOSTER, L. J., LENES, M. & SLOOF, L. H. (2008) Combined optical and electrical modeling of polymer: Fullerene bulk heterojunction solar cells. *J. Appl. Phys.* **103**, 084502.

[38] MARTIN, C. M., BURLAKOV, V. M. & ASSENDER, H. E. (2006) Modellng charge transport in composite solar cells. *Sol. Energy Mater. Sol. Cells* **90**, 900–915.

[39] MARTIN, C. M., BURLAKOV, V. M., ASSENDER, H. E. & BARKHOUSE, D. A. R. (2007) A numerical model for explaining the role of the interface morphology in composite solar cells. *J. Appl. Phys.* **102**, 104506.

[40] MARKOV, D. E., AMSTERDAM, E., BLOM, P. W. M., SIEVAL, A. B. & HUMMELEN, J. C. (2005) Accurate measurement of the exciton diffusion length in a conjugated polymer using a heterostructure with a side-chain cross-linked fullerene layer. *J. Phys. Chem. A* **109**, 5266–5274.

[41] MCNEILL, C. R., WESTENHOFF, S., GROVES, C., FRIEND, R. H. & GREENHAM, N. C. (2007) Influence of nanoscale phase separation on the charge generation dynamics and photovoltaic performance of conjugated polymer blends: Balancing charge generation and separation. *J. Phys. Chem. C* **111**, 19153–19160.

[42] NELSON, J. (2003) Diffusion-limited recombination in polymer-fullerene blends and its influence on photocurrent collection. *Phys. Rev. B* **67**, 155209.

[43] NELSON, J. (2003) *The Physics of Solar Cells*, London, Imperial College Press.

[44] OFFERMANS, T., MESKERS, S. C. J. & JANSSEN, R. A. J. (2005) Monte-Carlo simulations of geminate electron-hole pair dissociation in a molecular heterojunction: A two-step dissociation mechanism. *Chem. Phys.* **308**, 125–133.

[45] PAUTMEIER, L., RICHERT, R. & BÄSSLER, H. (1990) Poole-Frenkel behaviour of charge transport in organic solids with off-diagonal disorder studied by Monte Carlo simulation. *Synth. Met.* **37**, 271.

[46] PEUMANS, P., UCHIDA, S. & FORREST, S. R. (2003) Efficient bulk heterojunction photovoltaic cells using small-molecular-weight organic thin films. *Nature* **425**, 158–162.

[47] POTSCAVAGE, W. J., YOO, S. & KIPPELEN, B. (2008) Origin of the open-circuit voltage in a multilayer heterojunction organic solar cells. *Appl. Phys. Lett.* **93**, 193308.

[48] RICHARDSON, G., DENUAULT, G. & PLEASE, C. P. (2012) Multiscale modelling and analysis of lithium-ion battery charge and discharge. *J. Eng. Math.* **72**, 41–72.

[49] RICHARDSON, G., PLEASE, C. P., FOSTER, J. & KIRKPATRICK, J. A. (2012) Asymptotic solution of a model for bilayer organic diodes and solar cells. *SIAM J. Appl. Math.* **72**, 1792–1817.

[50] RICHARDSON, G. & CHAPMAN, S. J. (2011) Derivation of the bidomain equations for a beating heart with a general microstructure. *SIAM J. Appl. Math.* **71**, 657–675.

[51] SCOTT, J. C. & MALLIARAS, G. G. (1999) Charge injection and recombination at the metal-organic interface. *Chem. Phys. Lett.* **299**, 115–119.

[52] SEUNHYUP, Y., POTSCAVAGE, W. J., DOMERCQUA, B., LIC, T. D., JONES, S. C., SZOZSKIEWICZ, R., LEVIB, D., RIEDOC, E., MARDER, S. R. & KILLEN, B. (2007) Analysis of improved photovoltaic properties of pentacene/C60 organic solarcells: Effects of exciton blocking layer thickness and thermal annealing. *Solid-State Electron.* **51**, 1367.

[53] RAO, A., WILSON, M. W. B, HODGKISS, J. M., ALBERT-SEIFRIED, S., BÄSSLER, H. & FRIEND, R. H. (2010) Exciton fission and charge generation via triplet excitons in pentacene/$C_6$0 bilayers. *J. Am. Chem. Soc.* **132**, 12698–12703.

[54] SCHARFETTER, D. L. & GUMMEL, H. K. (1969) Large-signal analysis of a silicon Read diode oscillator. *IEEE Trans. Electron. Dev.* **16**, 64–77.

[55] SZE, S. M. & KWOK, K. NG (2006) *Physics of Semiconductor Devices*, 3rd ed., Wiley-Interscience, New York.

[56] TANSAE, C., BLOM, P. W. M., DE LEEUW, D. M. & MEIJER, E. J. (2004) Charge carrier density dependence of mobility in poly-p-phenylene vinylene. *Phys. Status Solidi B* **201**, 1236.

[57] VERLAAK, S., BELJONNE, D., CHEYNS, D., ROLIN, C., LINARES, M., CASTET, F., CORNIL, J. & HEREMANS, P. (2009) Electronic structure and geminate pair energetics at organic-organic interfaces: The case of pentacene/C_{60} heterojunctions. *Adv. Funct. Mater.* **19**, 3809–3814.

[58] WILLIAMS, J. & WALKER, A. B. (2008) Two-dimensional simulations of bulk heterojunction solar cell characteristics. *Nanotechnology* **19**, 424011.

[59] WAGENPFAHL, A., RAUH, D., BINDER, M., DEIBEL, C. & DYAKONOV, V. (2010) S-shaped current-voltage characteristics of organic solar devices. *Phys. Rev. B* **82**, 115306.

[60] YANG, F., SHTEIN, M. & FORREST, S. R. (2005) Controlled growth of a molecular bulk heterojunction photovoltaic cell. *Nat. Mat.* **4**, 37–41.